

Review paper: Virtual sources and their responses, Part II: data-driven single-sided focusing

Kees Wapenaar^{1*}, Jan Thorbecke¹, Joost van der Neut¹, Evert Slob¹
and Roel Snieder²

¹Department of Geoscience and Engineering, Delft University of Technology, PO Box 5048, 2600 GA Delft, The Netherlands, and ²Center for Wave Phenomena, Colorado School of Mines, Golden, CO 80401 USA

Received July 2016, revision accepted December 2016

ABSTRACT

In Part I of this paper, we defined a focusing wave field as the time reversal of an observed point-source response. We showed that emitting a time-reversed field from a closed boundary yields a focal spot that acts as an isotropic virtual source. However, when emitting the field from an open boundary, the virtual source is highly directional and significant artefacts occur related to multiple scattering. The aim of this paper is to discuss a focusing wave field, which, when emitted into the medium from an open boundary, yields an isotropic virtual source and does not give rise to artefacts. We start the discussion from a horizontally layered medium and introduce the single-sided focusing wave field in an intuitive way as an inverse filter. Next, we discuss single-sided focusing in two-dimensional and three-dimensional inhomogeneous media and support the discussion with mathematical derivations. The focusing functions needed for single-sided focusing can be retrieved from the single-sided reflection response and an estimate of the direct arrivals between the focal point and the accessible boundary. The focal spot, obtained with this single-sided data-driven focusing method, acts as an isotropic virtual source, similar to that obtained by emitting a time-reversed point-source response from a closed boundary.

Key words: Virtual source, Green's function retrieval, Multiples.

INTRODUCTION

In Part I of this paper, we reviewed the creation of virtual sources via time-reversal acoustics and seismic interferometry. These two methods, although distinct from a practical point of view, are based on the same theory, i.e., a representation of the homogeneous Green's function. In both methods, wave fields are focused onto a focal point, which subsequently acts as a virtual source. We concluded that accurate isotropic virtual sources can be created when the virtual-source position (i.e., the focal point) is illuminated from a boundary enclosing the medium. This requirement is a consequence of the fact that

the homogeneous Green's function representation is a closed boundary integral.

In many practical situations, the medium is accessible from one side only. This implies that, in practice, the virtual sources, created either with time-reversal acoustics or seismic interferometry, are far from being isotropic. Moreover, when the medium is inhomogeneous, artefacts occur as a result of the erroneous treatment of multiple scattering. The aim of Part II is to discuss how isotropic virtual sources, without scattering-related artefacts, can be created in inhomogeneous media in the situation that the medium is accessible from one side only. We start with a discussion of virtual sources in a horizontally layered medium, which explains the principle in an intuitive way. After this, we discuss the principle of single-sided focusing in 2D and 3D inhomogeneous media, following

*E-mail: c.p.a.wapenaar@tudelft.nl

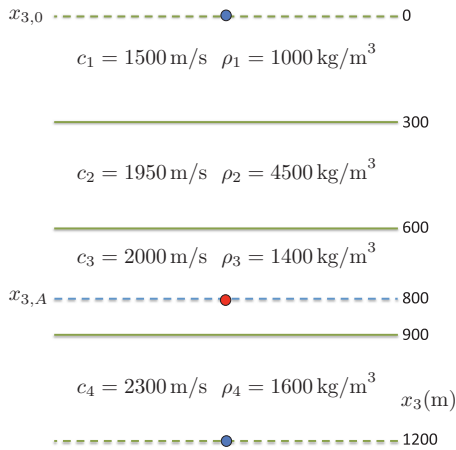


Figure 1 Horizontally layered medium with absorbing boundaries at the top and bottom. The red dot at $x_{3,A} = 800$ m indicates the source for the wave field in Fig. 2.

the same steps as for the horizontally layered medium, supported by mathematical derivations.

DISCUSSION OF VIRTUAL SOURCES IN A HORIZONTALLY LAYERED MEDIUM

Time-reversal acoustics

We review the principle of time-reversal acoustics using an example in a horizontally layered lossless medium. The reason for considering this simplified situation is that the evolution of the wave field through the medium can be followed in detail. This is helpful to understand why single-sided time-reversal acoustics fails to create isotropic virtual sources. This example serves as an introduction to explain in an intuitive way what is needed to create isotropic artefact-free virtual sources in media that can be accessed from one side only.

Consider the horizontally layered medium in Fig. 1, which is derived from a vertical cross section of the inhomogeneous medium in Fig. 1(a) in Part I, at horizontal position $x_1 = 0$, as a function of depth x_3 . The propagation velocities and mass densities of the layers are denoted by c_k and ρ_k , respectively, for $k = 1, 2, 3, 4$. The boundaries at the top ($x_3 = x_{3,0} = 0$ m) and bottom ($x_3 = 1200$ m) of the layered medium are absorbing (i.e., the half-spaces above and below these boundaries form a continuation of the first and last layers, respectively). Figure 2 shows the response to a source at depth $x_{3,A} = 800$ m (the red dot in Fig. 1). It is defined as $G(x_3, x_{3,A}, t) * s(t)$, where $G(x_3, x_{3,A}, t)$ is the Green's function

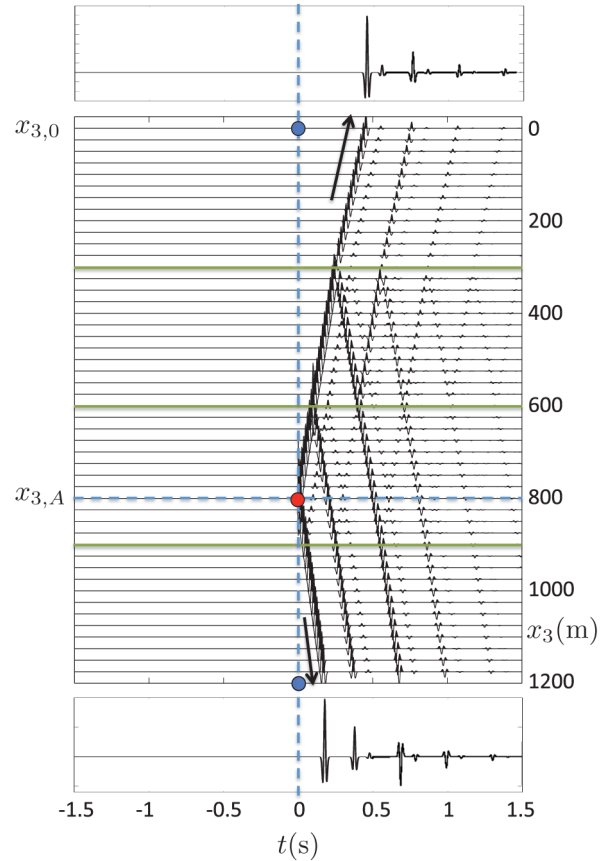


Figure 2 Green's function $G(x_3, x_{3,A}, t)$ convolved with source wavelet $s(t)$.

for fixed source depth $x_{3,A}$ and variable receiver depth x_3 and time t . Moreover, $s(t)$ is the source wavelet (here, a Ricker wavelet with a central frequency of 30 Hz), and the asterisk $*$ denotes convolution. The responses observed by receivers at the upper and lower boundaries (the blue dots in Fig. 1) are shown in the top and bottom panels in Fig. 2.

Figures 3, 4, and 5 are the 1D equivalents of the experiments discussed in Figs. 1, 3, and 4 in Part I. The top panel in Fig. 3 shows the time-reversed direct arrival of the Green's function observed at $x_{3,0} = 0$, which we denote as $G_d(x_{3,0}, x_{3,A}, -t) * s(-t)$. We denote the arrival time of the direct arrival as t_d ; hence, $G_d(x_{3,0}, x_{3,A}, -t)$ is an impulse at $t = -t_d$. This field is emitted into the medium by a source at $x_{3,0} = 0$. The evolution of this field through the layered medium is shown in the central panel in Fig. 3 as a function of depth and time, like in a vertical seismic profile. In this kind of display, it can be clearly seen how waves are reflected at the interfaces. Also, the entire paths of multiple reflections can be easily followed. The black line in the panel at the left

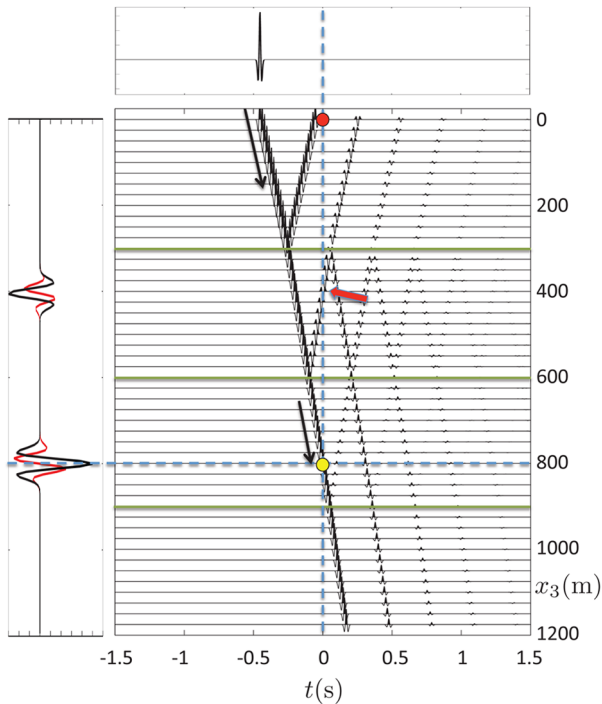


Figure 3 Emission of the time-reversed direct arrival, $G_d(x_{3,0}, x_{3,A}, -t) * s(-t)$, from the upper boundary into the horizontally layered medium. The virtual source at $x_{3,A} = 800$ m radiates only downward. Moreover, the virtual-source response for $t > 0$ is contaminated by the response to an undesired virtual source at approximately 400 m, indicated by the red arrow.

shows a cross section as a function of depth (x_3) for $t = 0$. It shows a band-limited focal spot at $x_{3,A} = 800$ m. This acts as a downward radiating (i.e., anisotropic) virtual source for the field at $t > 0$. In agreement with Part I, we denote this virtual-source function as $V_{1D}(x_3, x_{3,A})$ and we call the field for $t > 0$ the virtual-source response. The red line in the panel at the left shows a cross section of the temporal derivative of the central panel, also evaluated at $t = 0$. This is denoted as $\dot{V}_{1D}(x_3, x_{3,A})$. As explained in Part I, the two functions V_{1D} and \dot{V}_{1D} together form the virtual source in terms of initial conditions at $t = 0$, which uniquely define the response for $t > 0$ (here, the particular phase difference between the two functions causes the virtual source to be a downward radiating source). Note that the virtual-source functions also exhibit an artefact at a depth of approximately 400 m (similar to that in Fig. 1(e) in Part I). It is clear that this artefact is caused by the upgoing wave coming from the second interface, passing the $t = 0$ line at approximately 400 m (indicated by the red arrow in Fig. 3). This artefact acts as an undesired upward radiating virtual source, which contaminates the virtual-

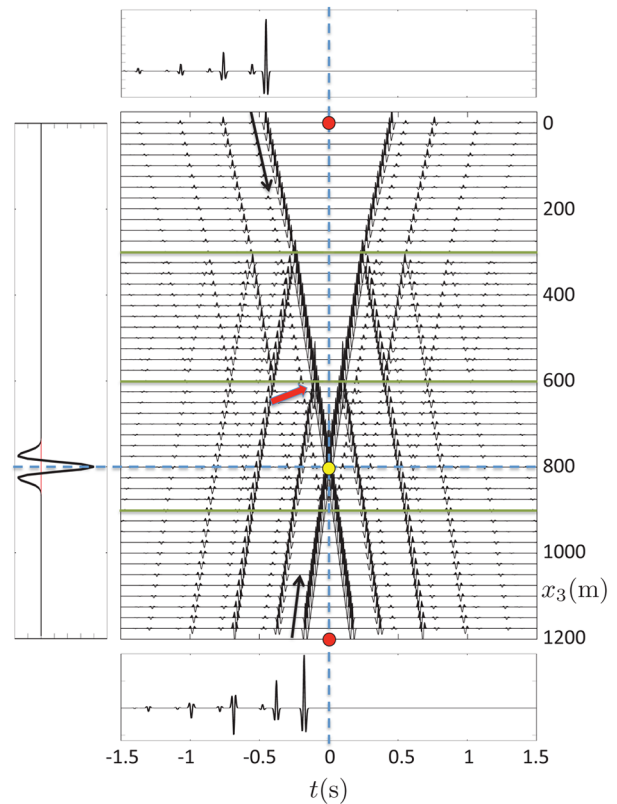


Figure 4 Emission of the time reversed responses from the upper and lower boundary into the horizontally layered medium. The virtual source at $x_{3,A} = 800$ m is purely isotropic and not contaminated by artefacts.

source response for $t > 0$ (ideally, the virtual-source response should be identical to the response to the actual source in Fig. 2).

In an ideal time-reversal experiment, the time-reversed field is emitted into the medium from all sides. For a horizontally layered medium, this means that the field should be emitted from the upper and lower boundaries. The top and bottom panels in Fig. 4 show the time reversals of the top and bottom panels in Fig. 2. These fields are emitted from both sides into the medium. The central panel in Fig. 4 shows the evolution of these fields through the medium (this is the 1D version of the 2D time-reversal experiment shown in Fig. 3 in Part I). It is shown how, for $t < 0$, downgoing and upgoing waves reach the interfaces from above and below, together giving rise to scattered waves in such a way that the field focuses at $t = 0$. For example, the red arrow indicates an upgoing wave arriving at the second interface in such a way that the upgoing wave above the second interface (the one indicated by the red arrow in Fig. 3) is annihilated. According to

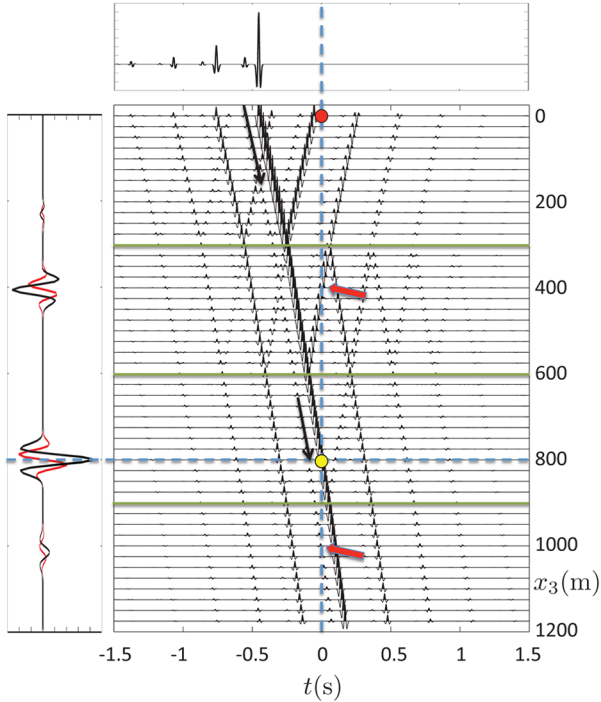


Figure 5 Emission of the time-reversed response from the upper boundary into the horizontally layered medium.

the theory discussed in Part I, the total wave field (for all t) is proportional to $G_h(x_3, x_{3,A}, t) * s(-t)$, where $G_h(x_3, x_{3,A}, t)$ is the homogeneous Green's function defined as

$$G_h(x_3, x_{3,A}, t) = G(x_3, x_{3,A}, t) + G(x_3, x_{3,A}, -t). \quad (1)$$

The field and its temporal derivative, both evaluated at $t = 0$, are shown by the black and red lines, respectively, in the left panel in Fig. 4. These are the virtual-source functions $V_{1D}(x_3, x_{3,A})$ and $\dot{V}_{1D}(x_3, x_{3,A})$. Note that the latter function vanishes for all x_3 . Together, these functions act as an isotropic (equally downward and upward radiating) virtual source for the field at $t > 0$ in the central panel of this figure. This virtual-source response accurately resembles the response to the actual source in Fig. 2.

With the total field being given by $G_h(x_3, x_{3,A}, t) * s(-t)$, the virtual-source functions follow from

$$V_{1D}(x_3, x_{3,A}) = [G_h(x_3, x_{3,A}, t) * s(-t)]_{t=0}, \quad (2)$$

$$\dot{V}_{1D}(x_3, x_{3,A}) = \left[\frac{\partial}{\partial t} \{G_h(x_3, x_{3,A}, t) * s(-t)\} \right]_{t=0}. \quad (3)$$

According to the theory in Part I, this gives for a symmetric source wavelet (like the Ricker wavelet used in this example)

$$V_{1D}(x_3, x_{3,A}) = \bar{\rho} \bar{c} s(r/\bar{c}), \quad (4)$$

$$\dot{V}_{1D}(x_3, x_{3,A}) = 0, \quad (5)$$

where $r = |x_3 - x_{3,A}|$. Here, \bar{c} and $\bar{\rho}$ are the propagation velocity and the mass density of the layer that contains the virtual source; hence, $\bar{c} = c_3 = 2000$ m/s and $\bar{\rho} = \rho_3 = 1400$ kg/m³. Equation (4) quantifies the black line in the left panel in Fig. 4 (which exhibits a scaled Ricker wavelet), and equation (5) confirms that the red line should indeed be zero (if it were not zero, the virtual source would not be isotropic).

Figure 5 shows the evolution of the field through the medium when the time-reversed response $G(x_{3,0}, x_{3,A}, -t) * s(-t)$ is emitted only from the upper boundary into the medium (this is the 1D version of the single-sided 2D time-reversal experiment shown in Fig. 4 in Part I). For $t < 0$, the scattering occurring at the interfaces in Fig. 5 is very different from that in Fig. 4 because the illumination from below is missing. Hence, unlike in Fig. 4, the field does not converge to a well-defined focus at $t = 0$. The left panel in Fig. 5, which shows the field (black line) and its derivative (red line) evaluated at $t = 0$, exhibits artefacts apart from the focal spot at $x_{3,A} = 800$ m (the red arrows in the central panel indicate the origin of some of these artefacts). These black and red lines form again the virtual-source functions $V_{1D}(x_3, x_{3,A})$ and $\dot{V}_{1D}(x_3, x_{3,A})$. The field for $t > 0$ in the central panel in Fig. 5 clearly shows that the virtual source is anisotropic and that its response is contaminated by artefacts, even more than in Fig. 3.

Figure 6(a), (b), and (c) shows an overview of traces involved in the time-reversal experiments that we discussed. Figure 6(a) is the response observed at the surface, i.e., $G(x_{3,0}, x_{3,A}, t) * s(t)$. Figure 6(b) is the time-reversed direct arrival of this response, i.e., $G_d(x_{3,0}, x_{3,A}, -t) * s(-t)$, whereas Fig. 6(c) is the time reversal of the full response; hence, $G(x_{3,0}, x_{3,A}, -t) * s(-t)$. In Figs. 3 and 5, we have shown that emitting either one of these time-reversed responses from the upper boundary into the medium yields anisotropic virtual sources, the responses of which are contaminated by scattering-related artefacts. Only when the time reversal of the full response is emitted from the upper and lower boundaries into the medium we obtain the desired isotropic artefact-free virtual-source response (Fig. 4).

Figure 6(d), (e), and (f) shows an overview of traces that will be discussed in the next section. We will show step by step that the trace in Fig. 6(f), when emitted from the upper

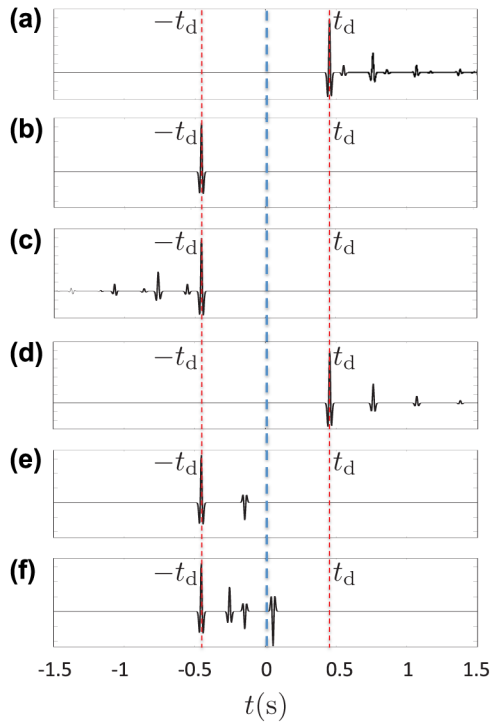


Figure 6 Traces involved in time-reversal acoustics and in single-sided focusing. (a) Response at the surface $G(x_{3,0}, x_{3,A}, t) * s(t)$. (b) Time-reversal of direct arrival, i.e., $G_d(x_{3,0}, x_{3,A}, -t) * s(-t)$. (c) Time-reversal of full response, i.e., $G(x_{3,0}, x_{3,A}, -t) * s(-t)$. (d) Transmission response $T(x_{3,A}, x_{3,0}, t) * s(t)$. (e) One-way focusing function $f_1^+(x_{3,0}, x_{3,A}, t) * s(t)$, with $f_1^+(x_{3,0}, x_{3,A}, t)$ being the inverse of $T(x_{3,A}, x_{3,0}, t)$. (f) Focusing function $\{f_1^+(x_{3,0}, x_{3,A}, t) - f_1^-(x_{3,0}, x_{3,A}, -t)\} * s(t)$, with $f_1^-(x_{3,0}, x_{3,A}, t)$ being the reflection response of $f_1^+(x_{3,0}, x_{3,A}, t)$.

boundary into the medium, also leads to the desired isotropic artefact-free virtual-source response. Note the difference between the traces in Fig. 6(c) and (f). They both have an event at $t = -t_d$, but apart from this, the trace in Fig. 6(c) is purely acausal, whereas that in Fig. 6(f) is purely causal: it consists of a pulse at $t = -t_d$, followed by a causal ‘‘coda’’.

Single-sided focusing functions

Here we discuss focusing as an inverse filtering process rather than a time-reversal process. Inverse filtering has a rich history in seismic data processing, starting with the early 1D inverse-filtering work of Robinson (1954) and Treitel and Robinson (1964). For 2D and 3D situations, seismic focusing of primary reflection data (seismic migration) has been formulated as an inverse filtering (or spatial deconvolution) process by Berkhout and van Wulfften Palthe (1979). Tanter,

Thomas and Fink (2000) used a similar inverse-filtering approach to design focusing wave fields as an alternative to time-reversal acoustics. Snieder, Sheiman and Calvert (2006) and Wapenaar, van der Neut and Ruigrok (2008) reformulated seismic interferometry as 1D and 2D/3D inverse-filtering (deconvolution) processes. Here we discuss a 1D inverse filter to create a virtual source in a horizontally layered medium that can be accessed from one side only. Later in this paper, we extend this approach to the 2D and 3D situations.

Consider again the horizontally layered medium in Fig. 1. We assume that the medium is accessible only at the upper boundary ($x_3 = x_{3,0}$), from which we want to emit a signal that focuses at $x_3 = x_{3,A}$. For the moment, we replace the medium below $x_{3,A}$ by a homogeneous half-space, i.e., we remove the third reflector at $x_3 = 900$ m and assume that, below this depth, the propagation velocity and mass density of the third layer (c_3 and ρ_3) are continued. We call this new medium the truncated medium (also often indicated as the reference medium). Note that, by its construction, the truncated medium is identical to the actual medium above $x_3 = x_{3,A}$, whereas it is homogeneous below this depth. We define the transmission response of the truncated medium as $T(x_{3,A}, x_{3,0}, t)$. This response, convolved with a source wavelet $s(t)$, is shown in Fig. 6(d). Note that the direct arrival occurs at $t = t_d$. We define a focusing function $f_1^+(x_3, x_{3,A}, t)$ that is incident on the truncated medium from the upper half-space and focuses at $x_3 = x_{3,A}$. Superscript + denotes that it is a downward propagating wave field, and the argument $x_{3,A}$ denotes the focal depth. We denote downward or upward propagating fields as ‘‘one-way’’ wave fields; hence, we call $f_1^+(x_3, x_{3,A}, t)$ a one-way focusing function. We define the focusing condition as

$$\delta(t) = T(x_{3,A}, x_{3,0}, t) * f_1^+(x_{3,0}, x_{3,A}, t). \quad (6)$$

This equation states that the one-way focusing function, when emitted into the truncated medium from $x_3 = x_{3,0}$, propagates to $x_3 = x_{3,A}$, where it collapses to a delta function. In terms of signal processing, equation (6) states that $f_1^+(x_{3,0}, x_{3,A}, t)$ is the inverse of $T(x_{3,A}, x_{3,0}, t)$. Figure 6(e) shows this focusing function, convolved with the wavelet $s(t)$. Note that the first arrival occurs at $t = -t_d$ and that the coda of this focusing function (in this case, a single pulse) is causal in the sense that it comes after the first arrival at $t = -t_d$. This is a general property of inverse transmission responses. It follows from two classical results, namely, (i) the transmission response of a horizontally layered medium is a delayed (by t_d) causal minimum-phase signal (Anstey and O’Doherty 1971; Robinson and Treitel 1976) and (ii) the inverse of a

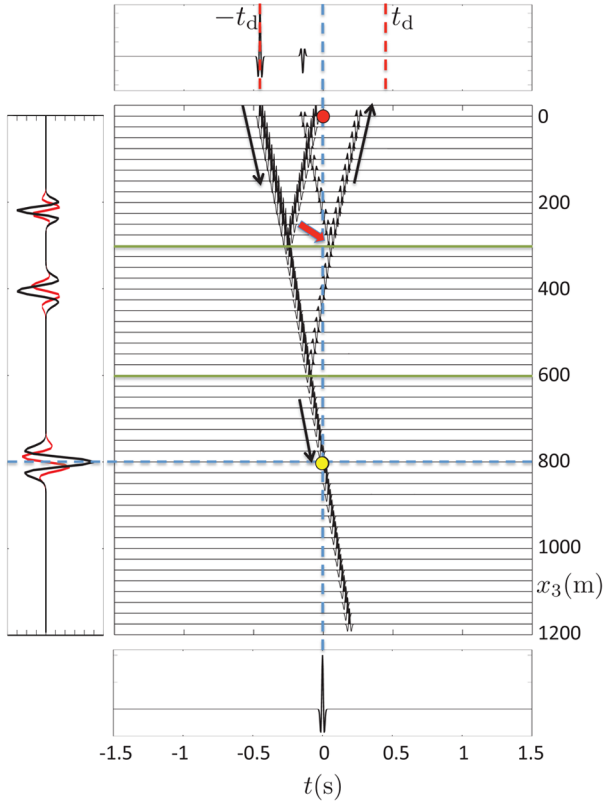


Figure 7 Emission of the one-way focusing function $f_1^+(x_{3,0}, x_{3,A}, t) * s(t)$ into the truncated medium.

minimum-phase signal is causal and minimum phase (Robinson 1954; Berkhout 1974).

Convolving both sides of equation (6) with wavelet $s(t)$ gives

$$s(t) = T(x_{3,A}, x_{3,0}, t) * \{f_1^+(x_{3,0}, x_{3,A}, t) * s(t)\}. \quad (7)$$

The top panel in Fig. 7 shows the focusing function $f_1^+(x_{3,0}, x_{3,A}, t)$, convolved with wavelet $s(t)$. This is emitted into the truncated medium from $x_3 = x_{3,0}$. The central panel in Fig. 7 shows the evolution of the field through the truncated medium. The red arrow indicates the second event of the focusing function arriving as a downgoing wave at the first reflector, exactly at the time that an upgoing wave arrives at this reflector from below. The amplitude of the incident downgoing wave is tuned such that there is no scattered downgoing wave leaving the first reflector at this time. As a consequence, only the first event of the focusing function reaches the focal depth $x_{3,A} = 800$ m. The field at this depth is shown in the bottom panel in Fig. 7. According to equation (7), it consists of the wavelet $s(t)$. This focused field acts as a virtual source for the downward propagating field in the half-space below

$x_{3,A} = 800$ m, as shown in the central panel in Fig. 7. We denote this temporal virtual-source function as $\Lambda_{1D}(t)$.

Note that the focusing experiment discussed here is essentially different from that in the previous examples. For clarity, we define two types of focusing conditions as follows:

- Focusing in depth: At constant time ($t = 0$), the focus $V_{1D}(x_3, x_{3,A})$ is proportional to the *spatial* wavelet $s(|x_3 - x_{3,A}|/\bar{c})$, and $\check{V}_{1D}(x_3, x_{3,A})$ is equal to zero (assuming the wavelet $s(t)$ is symmetric, see equations (4) and (5));
- Focusing in time: At constant depth ($x_3 = x_{3,A}$), the focus $\Lambda_{1D}(t)$ is proportional to the *temporal* wavelet $s(t)$ (see equation (7)).

The time-reversal experiment in Fig. 4 is an example of focusing in depth (at constant time), whereas Fig. 7 shows focusing in time (at constant depth).

Although emitting $f_1^+(x_{3,0}, x_{3,A}, t) * s(t)$ into the truncated medium leads to focusing in time, the panel on the left in Fig. 7 shows that focusing in depth is not achieved. The function $V_{1D}(x_3, x_{3,A})$ (black line) exhibits artefacts at shallow depths, and $\check{V}_{1D}(x_3, x_{3,A})$ (red line) is not zero. Next, we discuss the steps that lead to focusing in depth using focusing functions emitted from the upper boundary.

The first step aims at suppressing the artefacts in $V_{1D}(x_3, x_{3,A})$. Consider again the downgoing focusing function in Fig. 7 which, for variable depth x_3 , is denoted as $f_1^+(x_3, x_{3,A}, t)$. Before reaching the focus, a part of this focusing function is reflected upward. The upward reflected response is called $f_1^-(x_3, x_{3,A}, t)$. The two functions together constitute the two-way focusing function

$$f_1(x_3, x_{3,A}, t) = f_1^+(x_3, x_{3,A}, t) + f_1^-(x_3, x_{3,A}, t). \quad (8)$$

We take the upgoing response at the upper boundary and revert it in time, giving $f_1^-(x_{3,0}, x_{3,A}, -t)$. Due to the time reversal, this is again a downgoing field. We subtract it from the downgoing focusing function $f_1^+(x_{3,0}, x_{3,A}, t)$, which gives $f_1^+(x_{3,0}, x_{3,A}, t) - f_1^-(x_{3,0}, x_{3,A}, -t)$. This function, convolved with $s(t)$, is shown in the top panel in Fig. 8. It is emitted from $x_3 = x_{3,0}$ into the truncated medium (which is identical to the actual medium above the focal depth $x_{3,A}$ and homogeneous below this depth). The central panel in Fig. 8 shows the evolution of the field $\{f_1^+(x_3, x_{3,A}, t) - f_1^-(x_3, x_{3,A}, -t)\} * s(t)$ through the truncated medium. The red dashed lines indicate the direct waves. In the time interval between these lines, the upgoing response to the downgoing field is given by $\{f_1^-(x_3, x_{3,A}, t) - f_1^+(x_3, x_{3,A}, -t)\} * s(t)$. Here, the first term is the response to $f_1^+(x_{3,0}, x_{3,A}, t) * s(t)$ and the second term is the response to $-f_1^-(x_{3,0}, x_{3,A}, -t) * s(t)$. The superposition

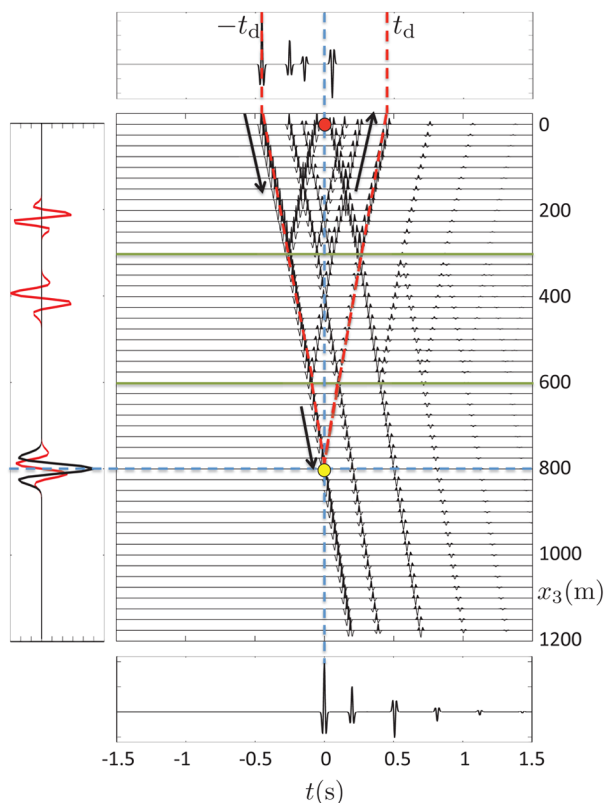


Figure 8 Emission of the focusing function $\{f_1^+(x_{3,0}, x_{3,A}, t) - f_1^-(x_{3,0}, x_{3,A}, -t)\} * s(t)$ into the truncated medium.

of the downgoing and upgoing fields between the red dashed lines consists of four terms that, using equation (8), can be simplified to $\{f_1(x_3, x_{3,A}, t) - f_1(x_3, x_{3,A}, -t)\} * s(t)$. Assuming a symmetric wavelet $s(t)$, this field is anti-symmetric in time; hence, at $t = 0$, it is zero. This is confirmed by the left panel in Fig. 8, in which $V_{1D}(x_3, x_{3,A})$ (the black line) is again the field of the central panel, evaluated at $t = 0$. It contains the focal spot around $x_{3,A} = 800$ m, but the artefacts that are present at shallower depths in $V_{1D}(x_3, x_{3,A})$ in Fig. 7 are absent in Fig. 8. The function $\tilde{V}_{1D}(x_3, x_{3,A})$ (the red line) is not zero (the artefacts at shallow depths are even stronger than those in Fig. 7). Hence, the focusing experiment in Fig. 8 partly accomplishes focusing in depth (for V_{1D} but not for \tilde{V}_{1D}). Note that the bottom panel in Fig. 8, which displays the field at the focal depth $x_{3,A} = 800$ m, shows that focusing in time no longer occurs. At the end of this section, we discuss the final step towards pure single-sided focusing in depth, but first, we investigate what happens when we emit $\{f_1^+(x_{3,0}, x_{3,A}, t) - f_1^-(x_{3,0}, x_{3,A}, -t)\} * s(t)$ into the actual medium instead of the truncated medium (see Fig. 9). By comparing the central panel carefully with that in Fig. 2, it appears that the response right of the rightmost red dashed

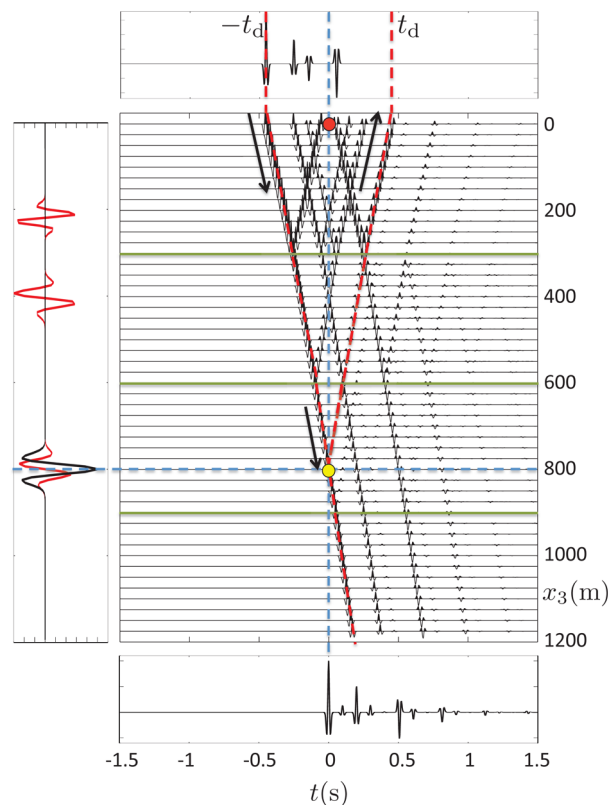


Figure 9 *Idem*, into the actual medium.

lines is equal to the Green's function $G(x_3, x_{3,A}, t)$, convolved with the source wavelet $s(t)$. In Fig. 7, it was already shown that the focal point at $x_{3,A} = 800$ m, created by the focusing function $f_1^+(x_{3,0}, x_{3,A}, t) * s(t)$, acts as a virtual source for downgoing waves. In Fig. 9, the virtual source at $x_{3,A}$ emits the same downgoing wave into the actual medium, which explains a part of the Green's function $G(x_3, x_{3,A}, t)$ right of the red dashed lines. The additional part of the focusing function in Fig. 9, i.e., $-f_1^-(x_{3,0}, x_{3,A}, -t) * s(t)$, generates additional events that (see right of the red dashed lines) behave as if they were radiated by a source for upgoing waves at $x_{3,A}$. Hence, the responses to $f_1^+(x_{3,0}, x_{3,A}, t) * s(t)$ and $-f_1^-(x_{3,0}, x_{3,A}, -t) * s(t)$ together form (see right of the red dashed lines) the isotropic virtual-source response $G(x_3, x_{3,A}, t) * s(t)$. The bottom panel in Fig. 9 shows again the field at the focal depth, i.e., $G(x_{3,A}, x_{3,A}, t) * s(t)$.

The focusing approach illustrated in Fig. 9 is due to Rose (2001, 2002). He showed that the focusing function at the upper boundary can be retrieved from the 1D reflection response measured at this boundary by solving the Marchenko equation in an iterative way. He called this method

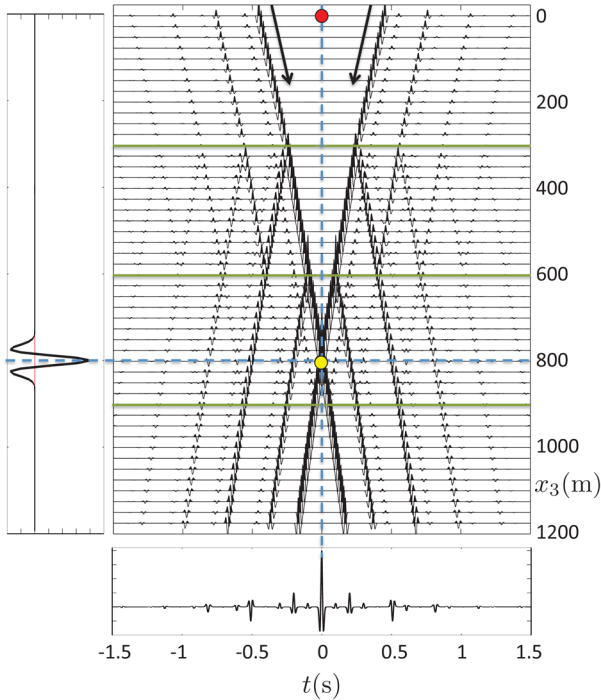


Figure 10 Superposition of Fig. 9 and its time reversal.

“single-sided autofocusing” because it requires no information about the medium other than its single-sided reflection response. Instead of focusing at a specific depth, his method focuses at “one-way travel time” t_d . The method is initiated with a pulse at $t = -t_d$, after which the coda of the focusing function (the top panel in Fig. 9) is retrieved with the iterative Marchenko scheme. Velocity information is only required if one wants to convert the one-way travel time (at which a focus occurs) to depth. For this purpose, a smooth velocity model suffices.

We now discuss the final step to achieve single-sided focusing in depth. This step aims at letting $\dot{V}_{1D}(x_3, x_{3,A})$ vanish. This function is defined as the temporal derivative of the field, evaluated at $t = 0$. Recall that the field in Figs. 8 and 9 in the region between the red dashed lines and above $x_{3,A}$ is given by the anti-symmetric function $\{f_1(x_3, x_{3,A}, t) - f_1(x_3, x_{3,A}, -t)\} * s(t)$. Hence, if we take the field at all (x_3, t) in Fig. 9 and add its time reversal to it, the field and its derivative vanish in this region (see Fig. 10). Outside this region, the same operation transforms the Green’s function $G(x_3, x_{3,A}, t) * s(t)$ into the homogeneous Green’s function $G_h(x_3, x_{3,A}, t) * s(t)$. The bottom panel in Fig. 10 shows $G_h(x_3, x_{3,A}, t) * s(t)$. This approach is due to Broggini and Snieder (2012).

Note that the result in Fig. 10 is identical to the time-reversal result in Fig. 4. However, whereas Fig. 4 was obtained by emitting the time-reversed responses from the upper and lower boundaries into the medium (the first of them shown in Fig. 6(c)), Fig. 10 was obtained by emitting a focusing function (Fig. 6(f)) only from the upper boundary into the medium and symmetrising the result by adding its time reversal. In the next section, we discuss the same steps for single-sided focusing in 2D and 3D media, this time supported by mathematical derivations.

SINGLE-SIDED FOCUSING IN TWO- AND THREE-DIMENSIONAL MEDIA

Focusing conditions in two- and three-dimensional media

In the 1D situation, we distinguished between (i) focusing in depth (at constant time) and (ii) focusing in time (at constant depth). For focusing in 2D and 3D inhomogeneous media, the additional coordinates to be considered, for both types of focusing, are the horizontal coordinates x_1 and x_2 (the latter only in the 3D case). Hence, from here onward, “focusing in depth” actually means “focusing in space” (at constant time), whereas “focusing in time” actually stands for “focusing in time and horizontal position” (at constant depth).

Focusing in depth (2D or 3D) at constant time is the type of focusing discussed in Part I. We defined the focal spot as the field of a focusing experiment evaluated at $t = 0$ and denoted this as $V(\mathbf{x}, \mathbf{x}_A)$, with $\mathbf{x} = (x_1, x_2, x_3)$ being the variable spatial coordinate vector and $\mathbf{x}_A = (x_{1,A}, x_{2,A}, x_{3,A})$ denoting the position of the focal point. Ideally, the focal spot $V(\mathbf{x}, \mathbf{x}_A)$ would be a spatial delta function $\delta(\mathbf{x} - \mathbf{x}_A)$ at $t = 0$, but this is never achieved in practice. The temporal derivative of the focused field, evaluated at $t = 0$, was denoted as $\dot{V}(\mathbf{x}, \mathbf{x}_A)$. The focused field and its derivative act as a virtual source in terms of initial conditions at $t = 0$ for the field at $t > 0$. For an ideal time-reversal experiment, assuming that the wavelet $s(t)$ is symmetric, we found

$$V_{3D}(\mathbf{x}, \mathbf{x}_A) = -\frac{\bar{\rho}}{2\pi r} \dot{s}(r/\bar{c}), \quad (9)$$

$$V_{2D}(\mathbf{x}, \mathbf{x}_A) = -\frac{\bar{\rho}}{\pi} \int_{r/\bar{c}}^{\infty} \frac{\dot{s}(t)}{\sqrt{t^2 - r^2/\bar{c}^2}} dt, \quad (10)$$

and $\dot{V}(\mathbf{x}, \mathbf{x}_A) = 0$ for both cases, where $r = |\mathbf{x} - \mathbf{x}_A|$ and $\dot{s}(t)$ denotes the temporal derivative of $s(t)$.

Focusing in time (2D or 3D) at constant depth is a generalisation of the type of focusing illustrated in the 1D experiment in Fig. 7. The focal spot is defined as the field of

a focusing experiment evaluated at the focal depth $x_3 = x_{3,A}$. It is denoted as $\Lambda(\mathbf{x}_H, \mathbf{x}_{H,A}, t)$, with $\mathbf{x}_H = (x_1, x_2)$ being the variable horizontal coordinate vector and $\mathbf{x}_{H,A} = (x_{1,A}, x_{2,A})$ denoting the horizontal position of the focal point. Ideally, the focal spot $\Lambda(\mathbf{x}_H, \mathbf{x}_{H,A}, t)$ would be a product of spatial and temporal delta functions, i.e., $\delta(\mathbf{x}_H - \mathbf{x}_{H,A})\delta(t)$ at $x_3 = x_{3,A}$. In practice, the ideal focal spot is never achieved, as we will see in the next section. The focused field acts as a virtual source in terms of a boundary condition at $x_3 = x_{3,A}$ for the field at $x_3 > x_{3,A}$.

Focusing in time

Similar as for the 1D example discussed in Fig. 7, we start by introducing a truncated medium (also often called a reference medium), which is identical to the actual medium above the depth level $x_3 = x_{3,A}$ of the focal point \mathbf{x}_A and homogeneous at and below this depth level. We also assume that the actual medium is homogeneous at and above the upper boundary $x_3 = x_{3,0} = 0$. For the inhomogeneous medium in Fig. 1(a) in Part I, the truncated medium is shown in Fig. 11(a). We denote the upper boundary at $x_3 = 0$ as $\partial\mathbb{D}_0$, whereas we denote the depth level $x_3 = x_{3,A}$ of the focal point as $\partial\mathbb{D}_A$. Similar as in the 1D example, we define a one-way focusing function $f_1^+(\mathbf{x}, \mathbf{x}_A, t)$, which, for \mathbf{x} on $\partial\mathbb{D}_0$, is defined as the inverse of the transmission response between $\partial\mathbb{D}_0$ and \mathbf{x}_A . Hence, when $f_1^+(\mathbf{x}, \mathbf{x}_A, t)$ is emitted from the upper boundary into the truncated medium, it focuses at \mathbf{x}_A . This is illustrated in Fig. 11. Figure 11(b) shows $f_1^+(\mathbf{x}, \mathbf{x}_A, t) * s(t)$ as a function of \mathbf{x} (on $\partial\mathbb{D}_0$) and t (here, $s(t)$ is again a Ricker wavelet with a central frequency of 30 Hz). This focusing function consists of an event at $-t_d(\mathbf{x}_A, \mathbf{x})$, followed by a coda, which, in this case, consists of a single event. Here, $t_d(\mathbf{x}_A, \mathbf{x})$ denotes a travel-time curve, indicating the direct arrival of the transmission response between \mathbf{x} (on $\partial\mathbb{D}_0$) and \mathbf{x}_A . Hence, similar as in the 1D example in Fig. 7, the first event of the focusing function occurs at minus the direct arrival time of the transmission response. The rays in Fig. 11(a) illustrate the propagation of the focusing function through the medium. The outer red rays represent the propagation of the first event of $f_1^+(\mathbf{x}, \mathbf{x}_A, t) * s(t)$ to the focal point at \mathbf{x}_A . The upgoing blue rays represent the reflected focusing function $f_1^-(\mathbf{x}, \mathbf{x}_A, t) * s(t)$. These upgoing rays would cause new downgoing rays at the first interface if they were not met by additional downgoing rays (the inner red rays in the first layer), coming from the coda of $f_1^+(\mathbf{x}, \mathbf{x}_A, t) * s(t)$. These downgoing rays are tuned such that no downgoing rays are leaving the first interface; hence, the outer red rays are the only ones reaching the focal plane $\partial\mathbb{D}_A$ (a similar mechanism

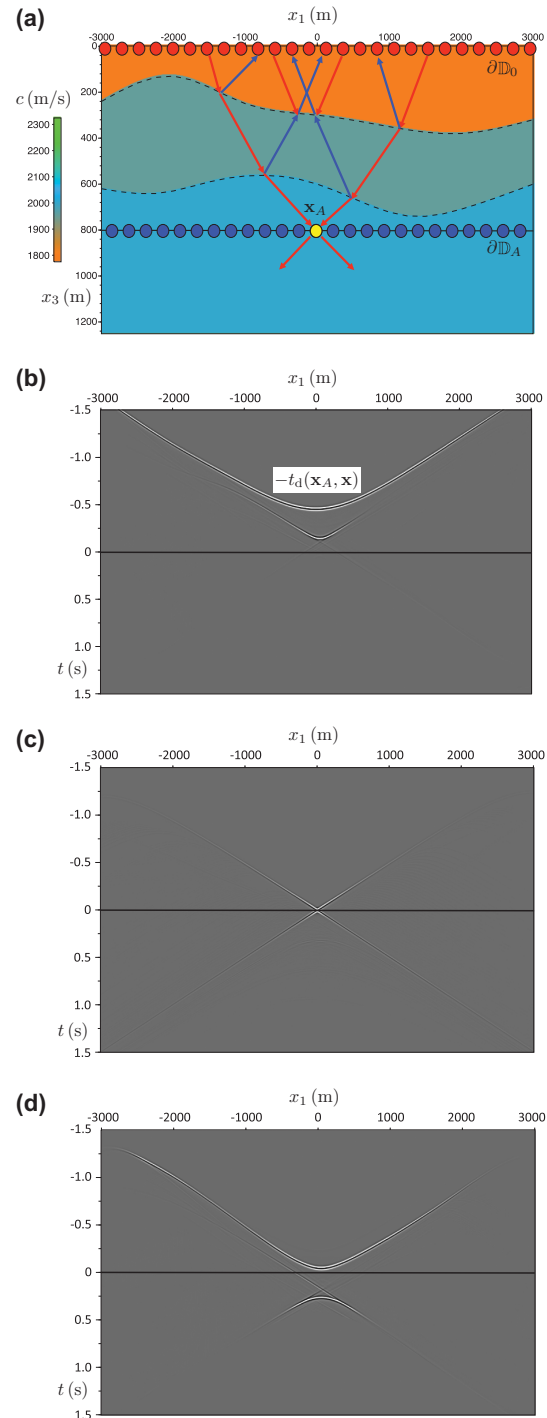


Figure 11 (a) Emission of the one-way focusing function into the truncated medium. (b) The downgoing focusing function $f_1^+(\mathbf{x}, \mathbf{x}_A, t) * s(t)$ for all \mathbf{x} at the upper boundary $\partial\mathbb{D}_0$. (c) *Idem*, for all \mathbf{x} at the focal plane $\partial\mathbb{D}_A$. This is a focus in time and horizontal position (at constant depth). (d) The upgoing focusing function $f_1^-(\mathbf{x}, \mathbf{x}_A, t) * s(t)$ for all \mathbf{x} at the upper boundary $\partial\mathbb{D}_0$.

for the 1D focusing function was explained in the discussion of Fig. 7). Figure 11(c) shows the focused field that would be observed when receivers would be present at the focal plane $\partial\mathbb{D}_A$, i.e., it shows $f_1^+(\mathbf{x}, \mathbf{x}_A, t) * s(t)$ as a function of \mathbf{x} on $\partial\mathbb{D}_A$ and t . We define the focal spot as the vertical derivative of this function, evaluated at $x_3 = x_{3,A}$; hence

$$\Lambda(\mathbf{x}_H, \mathbf{x}_{H,A}, t) = \left[\partial_3 f_1^+(\mathbf{x}, \mathbf{x}_A, t) * s(t) \right]_{x_3=x_{3,A}}. \quad (11)$$

The vertical derivative is taken here to be consistent with our earlier definition of the focusing function (Wapenaar *et al.* 2014) (it facilitates its use in the reciprocity theorems in the theoretical derivations in the Appendix and it causes the wavenumber spectrum of the focal spot to be flat for the propagating wavefield). Figure 11(c) shows that the focal spot is a band-limited version of a delta function at $\mathbf{x}_H = \mathbf{x}_{H,A}$ and $t = 0$. The band limitation is due to the band-limited wavelet $s(t)$ and the negligence of evanescent waves (Berkhout and van Wulfften Palthe 1979; Thomson, Kitchenside and Fletcher 2016). Finally, Fig. 11(d) shows the reflected focusing function $f_1^-(\mathbf{x}, \mathbf{x}_A, t) * s(t)$ for \mathbf{x} on $\partial\mathbb{D}_0$.

There are several ways to obtain the focusing function in practice. When the medium is known, its transmission response can be modelled and subsequently inverted. We call this a model-driven approach. Alternatively, to avoid inversion of the transmission response, the focusing function can be modelled directly, following a recursive Kirchhoff–Helmholtz wavefield extrapolation approach (Wapenaar 1993; Becker *et al.* 2016), starting with the focused field at $\partial\mathbb{D}_A$ and recursively moving upward. This gives $f_1^+(\mathbf{x}, \mathbf{x}_A, t)$ and $f_1^-(\mathbf{x}, \mathbf{x}_A, t)$ for all \mathbf{x} above $\partial\mathbb{D}_A$. This is also a model-driven approach. With our recent work on the 2D and 3D Marchenko methods, we have shown that these functions can also be derived from reflection measurements at the upper boundary (Wapenaar *et al.* 2013; Slob *et al.* 2014; van der Neut *et al.* 2015c). This data-driven approach (which was actually used to obtain Fig. 11(b) and 11(d)) is briefly reviewed in a later section. Before we come to this, we discuss the steps that are needed to go from focusing in time to focusing in depth.

From focusing in time to focusing in depth

In the 1D examples, we discussed step by step how the focusing-in-time experiment (Fig. 7) was turned into a focusing-in-depth experiment (Fig. 10). Here, we discuss similar steps for the 2D and 3D situations. To this end, we first define Green's functions and focusing functions in a more formal way and discuss their mutual relations (which are derived

in the Appendix). Based on these relations, we discuss the steps needed to go from focusing in time to focusing in depth.

We introduce a Green's function $G(\mathbf{x}, \mathbf{x}_R, t)$ in the actual medium for a source at \mathbf{x}_R just above the upper boundary $\partial\mathbb{D}_0$ (hence, $\mathbf{x}_R = (\mathbf{x}_{H,R}, x_{3,0} - \epsilon)$, with $\epsilon \rightarrow 0$). This Green's function obeys wave equation (A-5) in Appendix A in Part I (with \mathbf{x}_A replaced by \mathbf{x}_R). We decompose this Green's function into downgoing and upgoing components according to

$$G(\mathbf{x}, \mathbf{x}_R, t) = G^+(\mathbf{x}, \mathbf{x}_R, t) + G^-(\mathbf{x}, \mathbf{x}_R, t). \quad (12)$$

Because the half-space at and above $\partial\mathbb{D}_0$ is homogeneous, the downgoing field at $\partial\mathbb{D}_0$ consists only of the direct field just below the point source, which is given by

$$\left[\partial_3 G^+(\mathbf{x}, \mathbf{x}_R, t) \right]_{x_3=x_{3,0}} = -\frac{1}{2} \rho(\mathbf{x}_R) \delta(\mathbf{x}_H - \mathbf{x}_{H,R}) \dot{\delta}(t). \quad (13)$$

See equation (A-5) in the Appendix. The upgoing field at $\partial\mathbb{D}_0$ is proportional to the reflection response of the half-space below $\partial\mathbb{D}_0$, according to

$$\left[\partial_3 G^-(\mathbf{x}, \mathbf{x}_R, t) \right]_{x_3=x_{3,0}} = \left[\frac{1}{2} \rho(\mathbf{x}) \dot{R}(\mathbf{x}_R, \mathbf{x}, t) \right]_{x_3=x_{3,0}}. \quad (14)$$

See equation (A-6) in the Appendix.

The one-way focusing functions, informally introduced in the previous section, form the downgoing and upgoing parts of the two-way focusing function $f_1(\mathbf{x}, \mathbf{x}_A, t)$ according to

$$f_1(\mathbf{x}, \mathbf{x}_A, t) = f_1^+(\mathbf{x}, \mathbf{x}_A, t) + f_1^-(\mathbf{x}, \mathbf{x}_A, t). \quad (15)$$

At the focal plane $\partial\mathbb{D}_A$, the downgoing part of the focusing function ideally obeys the following relation:

$$\left[\partial_3 f_1^+(\mathbf{x}, \mathbf{x}_A, t) \right]_{x_3=x_{3,A}} = -\frac{1}{2} \rho(\mathbf{x}_A) \delta(\mathbf{x}_H - \mathbf{x}_{H,A}) \dot{\delta}(t). \quad (16)$$

The factor $-\frac{1}{2} \rho(\mathbf{x}_A)$ and the differentiation of the delta function (denoted by the dot) are included for consistency with equation (13). To avoid instability caused by the evanescent field, the spatial delta function should be interpreted in a band-limited sense (the effect of this band limitation is shown in Fig. 11(c)). Recall that the focusing function is defined in the truncated medium, which is identical to the actual medium above the focal plane $\partial\mathbb{D}_A$ but homogeneous below this plane. As a consequence, the upgoing part of the focusing function and its derivative vanish at and below $\partial\mathbb{D}_A$. Hence, next to equation (16), we have

$$\left[\partial_3 f_1^-(\mathbf{x}, \mathbf{x}_A, t) \right]_{x_3=x_{3,A}} = 0. \quad (17)$$

Unlike the Green's function, the focusing function obeys a wave equation without a delta function on the right-hand side. Hence, the focal point \mathbf{x}_A is not a sink; below the focal

depth, the focusing function $f_1^+(\mathbf{x}, \mathbf{x}_A, t)$ continues propagating downward.

In the Appendix, we derive the following relations between the Green's functions and the focusing functions

$$\begin{aligned} G^-(\mathbf{x}_A, \mathbf{x}_R, t) + f_1^-(\mathbf{x}_R, \mathbf{x}_A, t) \\ = \int_{\partial\mathbb{D}_0} d^2\mathbf{x} \int_{-\infty}^t R(\mathbf{x}_R, \mathbf{x}, t-t') f_1^+(\mathbf{x}, \mathbf{x}_A, t') dt' \end{aligned} \quad (18)$$

and

$$\begin{aligned} G^+(\mathbf{x}_A, \mathbf{x}_R, t) - f_1^+(\mathbf{x}_R, \mathbf{x}_A, -t) \\ = - \int_{\partial\mathbb{D}_0} d^2\mathbf{x} \int_{-\infty}^t R(\mathbf{x}_R, \mathbf{x}, t-t') f_1^-(\mathbf{x}, \mathbf{x}_A, -t') dt'. \end{aligned} \quad (19)$$

The upper integration boundary $t' = t$ of the time integrals accounts for the causality of the reflection response $R(\mathbf{x}_R, \mathbf{x}, t-t')$. Adding these equations and using source-receiver reciprocity for the Green's function gives

$$\begin{aligned} G(\mathbf{x}_R, \mathbf{x}_A, t) - f_2(\mathbf{x}_A, \mathbf{x}_R, -t) \\ = \int_{\partial\mathbb{D}_0} d^2\mathbf{x} \int_{-\infty}^t R(\mathbf{x}_R, \mathbf{x}, t-t') f_2(\mathbf{x}_A, \mathbf{x}, t') dt', \end{aligned} \quad (20)$$

with

$$f_2(\mathbf{x}_A, \mathbf{x}, t) = f_1^+(\mathbf{x}, \mathbf{x}_A, t) - f_1^-(\mathbf{x}, \mathbf{x}_A, -t). \quad (21)$$

We previously introduced $f_2(\mathbf{x}_A, \mathbf{x}, t)$ as a focusing function that has its focal plane at $\partial\mathbb{D}_0$ (Wapenaar *et al.* 2014). Here, we merely use f_2 as a compact notation for the combination of the one-way focusing functions f_1^+ and f_1^- , as defined in equation (21).

The right-hand side of equation (20) represents the application of the reflection response $R(\mathbf{x}_R, \mathbf{x}, t)$ at the upper boundary $\partial\mathbb{D}_0$ to the function $f_2(\mathbf{x}_A, \mathbf{x}, t)$ for \mathbf{x} at $\partial\mathbb{D}_0$. According to equation (21), this function consists of the downgoing focusing function $f_1^+(\mathbf{x}, \mathbf{x}_A, t)$ for all \mathbf{x} at $\partial\mathbb{D}_0$ (Fig. 11(b)) and the time reversal of the reflected focusing function $f_1^-(\mathbf{x}, \mathbf{x}_A, t)$ (Fig. 11(d)), which, because of the time reversal, is also a downgoing field at $\partial\mathbb{D}_0$. This total downgoing field at $\partial\mathbb{D}_0$, convolved with a symmetric wavelet $s(t)$, is shown in Fig. 12(a). It consists of an event at $-t_d(\mathbf{x}_A, \mathbf{x})$ (just above the red dashed line), followed by a coda. The left-hand side of equation (20) is the reflection response of the medium to the downgoing field $f_2(\mathbf{x}_A, \mathbf{x}, t)$. It consists of the time reversal of $-f_2(\mathbf{x}_A, \mathbf{x}_R, t)$ (which is an upgoing field) and the Green's function $G(\mathbf{x}_R, \mathbf{x}_A, t)$, which is the response to a virtual source at the position of the focal point, \mathbf{x}_A , observed at \mathbf{x}_R at the upper boundary $\partial\mathbb{D}_0$. Because the half-space above $\partial\mathbb{D}_0$ is homogeneous, this Green's function is also an upgoing field

at $\partial\mathbb{D}_0$. The total upgoing field at $\partial\mathbb{D}_0$ convolved with the symmetric wavelet $s(t)$, i.e., the left-hand side of equation (20), is shown in Fig. 12(b).

Figure 13 shows the evolution of this field through the medium. This figure was obtained by emitting $f_2(\mathbf{x}_A, \mathbf{x}, t) * s(t)$ from the boundary $\partial\mathbb{D}_0$ into a model of the medium. The snapshots for $t < 0$ show a field converging to the focal point at \mathbf{x}_A . The snapshot at $t = 0$ shows the virtual-source function (or focal spot) $V_{2D}(\mathbf{x}, \mathbf{x}_A)$. Finally, the snapshots for $t > 0$ show a field propagating away from the virtual source at \mathbf{x}_A . Similar as in the 1D experiment in Fig. 9, we observe that the virtual-source function $V_{2D}(\mathbf{x}, \mathbf{x}_A)$ in Fig. 13(c) is nicely concentrated around the focal point \mathbf{x}_A . Hence, similar as in Fig. 9, we have made a step towards focusing in depth. However, the snapshots at $t = -0.03$ and $t = +0.03$ seconds (Fig. 13(b) and (d)) show considerable artefacts at shallower depths. These artefacts appear to have opposite signs. Hence, $\dot{V}_{2D}(\mathbf{x}, \mathbf{x}_A)$, which is roughly proportional to the difference of the snapshots at $t = +0.03$ and $t = -0.03$ seconds, does not vanish.

The final step towards pure single-sided focusing in depth aims at letting $\dot{V}_{2D}(\mathbf{x}, \mathbf{x}_A)$ vanish. This is achieved in a similar way as in the 1D experiment, where we superposed Fig. 9 and its time reversal to obtain Fig. 10 (Broggini and Snieder 2012). Here, we superpose one by one the snapshots at negative times (Fig. 13(c), (b), and (a)) to the snapshots at the corresponding positive times (Fig. 13(c), (d), and (e)), yielding the snapshots in Fig. 14(a), (b), and (c). The snapshot at $t = 0$ (see Fig. 14(a)) represents the virtual-source function $V_{2D}(\mathbf{x}, \mathbf{x}_A)$. It is quantified by equation (10) and illustrated in Fig. 6(b) in Part I. Given that the artefacts in the snapshots at $t = -0.03$ and $t = +0.03$ seconds (Fig. 13(b) and (d)) have opposite signs, the superposition of these snapshots makes these artefacts cancel each other (Fig. 14(b)). Moreover, the wavefront just above the virtual source at \mathbf{x}_A in Fig. 13(b), added to the wavefront just below the virtual source in Fig. 13(d), approximates the response to an isotropic virtual source (Fig. 14(b)). A similar reasoning holds for the other snapshots in Fig. 14 and for those at negative times (not shown in Fig. 14). The result is the homogeneous Green's function $G_h(\mathbf{x}, \mathbf{x}_A, t) * s(t) = \{G(\mathbf{x}, \mathbf{x}_A, t) + G(\mathbf{x}, \mathbf{x}_A, -t)\} * s(t)$, for which $\dot{V}_{2D}(\mathbf{x}, \mathbf{x}_A)$ indeed vanishes. The retrieval of the homogeneous Green's function can be mathematically justified as follows. At the upper boundary, the incident field is $f_2(\mathbf{x}_A, \mathbf{x}, t) * s(t) = \{f_1^+(\mathbf{x}, \mathbf{x}_A, t) - f_1^-(\mathbf{x}, \mathbf{x}_A, -t)\} * s(t)$ (Fig. 12(a)) and its response is $\{G(\mathbf{x}_R, \mathbf{x}_A, t) - f_2(\mathbf{x}_A, \mathbf{x}_R, -t)\} * s(t)$ (Fig. 12(b)). Hence, setting $\mathbf{x} = \mathbf{x}_R$, the total field at $\partial\mathbb{D}_0$ is $\{f_1^+(\mathbf{x}_R, \mathbf{x}_A, t) - f_1^-(\mathbf{x}_R, \mathbf{x}_A, -t) + G(\mathbf{x}_R, \mathbf{x}_A, t) - f_1^+(\mathbf{x}_R, \mathbf{x}_A, -t) + f_1^-(\mathbf{x}_R, \mathbf{x}_A, t)\} * s(t)$. Adding to this its

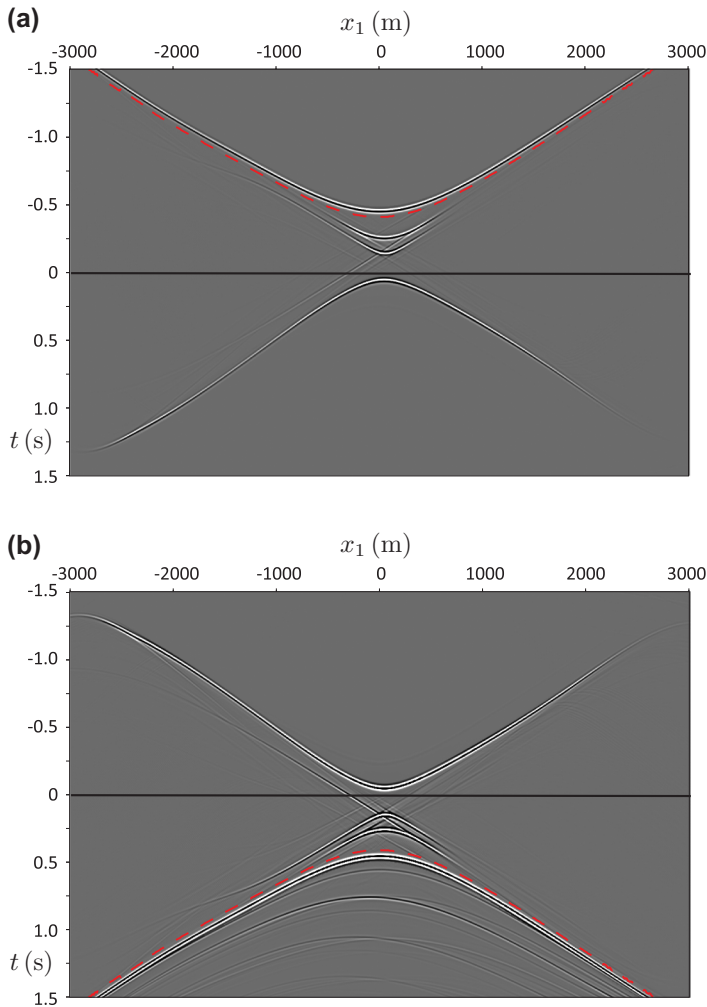


Figure 12 (a) The downgoing field $f_2(\mathbf{x}_A, \mathbf{x}, t) * s(t) = \{f_1^+(\mathbf{x}, \mathbf{x}_A, t) - f_1^-(\mathbf{x}, \mathbf{x}_A, -t)\} * s(t)$ for all \mathbf{x} at the upper boundary $\partial\mathbb{D}_0$. (b) The reflection response to $f_2(\mathbf{x}_A, \mathbf{x}, t) * s(t)$ at the upper boundary $\partial\mathbb{D}_0$. According to equation (20), this consists of the time reversal of $f_2(\mathbf{x}_A, \mathbf{x}_R, t) * s(t)$ (of which the coda resides above the red dashed line) and the Green's function $G(\mathbf{x}_R, \mathbf{x}_A, t) * s(t)$ (residing entirely below the red dashed line).

time reversal, using the assumption that $s(t)$ is a symmetric wavelet, all the focusing functions cancel each other. What remains is the homogeneous Green's function $G_h(\mathbf{x}_R, \mathbf{x}_A, t) * s(t) = \{G(\mathbf{x}_R, \mathbf{x}_A, t) + G(\mathbf{x}_R, \mathbf{x}_A, -t)\} * s(t)$.

It is striking that the result in Fig. 14 is nearly identical to that in Fig. 3 in Part I. However, whereas the result in Fig. 3 in Part I was obtained by emitting a time-reversed Green's function from an enclosing boundary into the medium, Fig. 14 has been obtained by emitting a focusing function only from the upper boundary into the medium (Fig. 13) and superposing its time reversal to this.

It should be noted that, for this numerical example, the focusing function was available at the upper boundary from $x_1 = -3000$ m to $x_1 = +3000$ m (see Figs. 11 and 12), which was necessary to obtain the almost perfect isotropic virtual

source in Fig. 14. In practice, the focusing function will usually be available at a smaller part of the upper boundary, meaning that the retrieved virtual source will not be perfectly isotropic. In particular, it will not radiate at large angles; however, it will equally radiate downgoing and upgoing waves. From here onward, the term “isotropic virtual source” stands for a virtual source that radiates downgoing and upgoing waves with approximately constant amplitudes under a significant range of angles.

In the next section, we show (i) that the focusing functions can be retrieved from the reflection response at the upper boundary and (ii) that a virtual-source response like the one in Fig. 14 can be retrieved from the focusing functions and the reflection response at the upper boundary (instead of by emitting the focusing function, physically or numerically, into a medium).

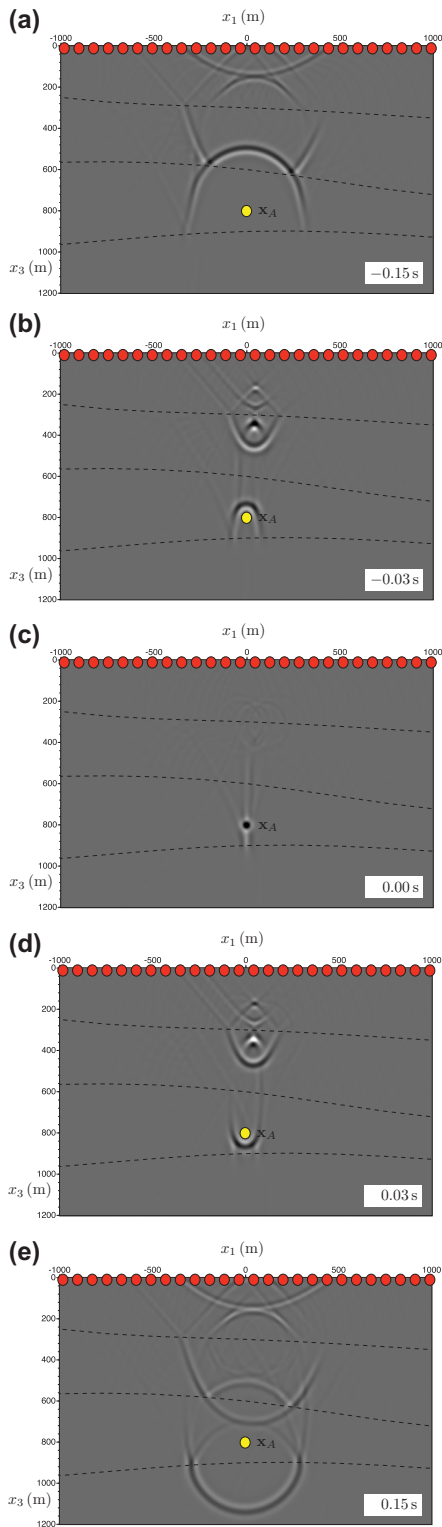


Figure 13 Emission of the focusing function $f_2(\mathbf{x}_A, \mathbf{x}, t) * s(t)$ from the upper boundary into the actual medium.

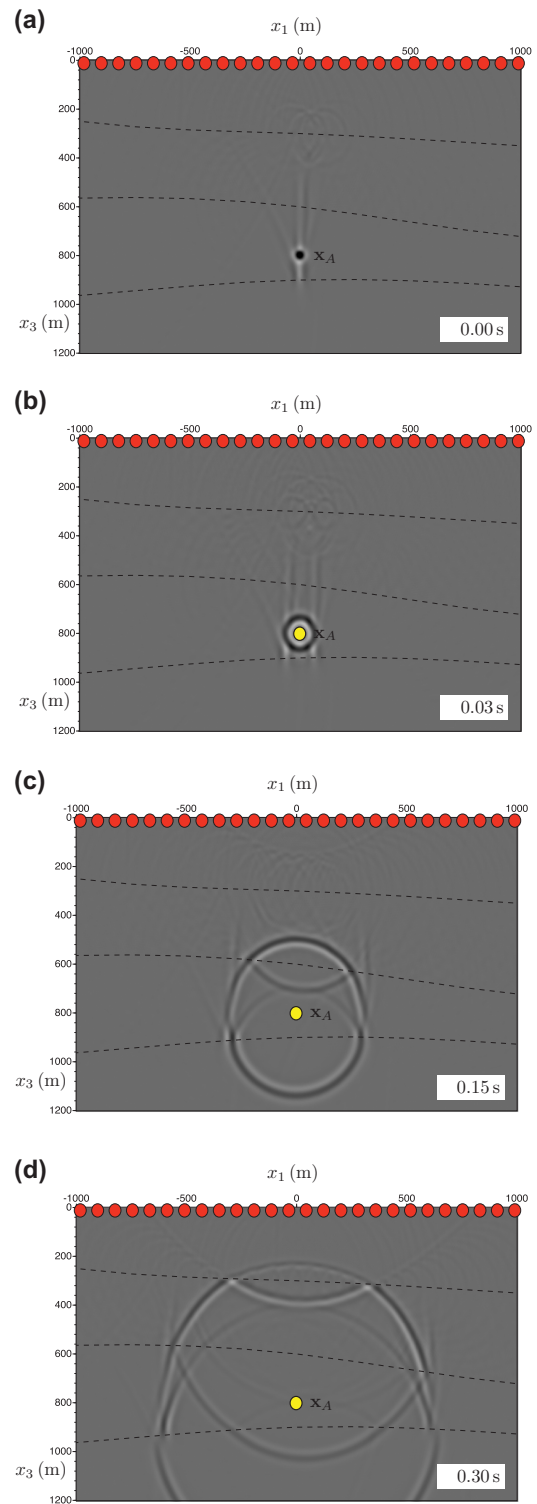


Figure 14 One-by-one superposition of the snapshots in Fig. 13 at negative times to those at the corresponding positive times. The snapshot at $t = 0$ is a focus in depth (at constant time).

DATA-DRIVEN SINGLE-SIDED FOCUSING IN TWO- AND THREE-DIMENSIONAL MEDIA

The Marchenko method: data-driven retrieval of the focusing function

Consider the left-hand side of equation (20), i.e., the response $G(\mathbf{x}_R, \mathbf{x}_A, t) - f_2(\mathbf{x}_A, \mathbf{x}_R, -t)$. This function, convolved with a wavelet, is shown in Fig. 12(b). The red dashed line in this figure denotes the travel time of the direct arrival, i.e., $t_d(\mathbf{x}_A, \mathbf{x}_R)$ (fixed \mathbf{x}_A , variable \mathbf{x}_R), minus a small value ϵ , approximately equal to half the duration of the symmetric wavelet $s(t)$. Hence, the Green's function convolved with the wavelet, i.e., $G(\mathbf{x}_R, \mathbf{x}_A, t) * s(t)$, resides entirely in the region $t > t_d^\epsilon(\mathbf{x}_A, \mathbf{x}_R) = t_d(\mathbf{x}_A, \mathbf{x}_R) - \epsilon$, i.e., below the red dashed line. Since $f_2(\mathbf{x}_A, \mathbf{x}_R, t)$ consists of an event at $-t_d(\mathbf{x}_A, \mathbf{x}_R)$, followed by a coda, the time reversal of the coda of $f_2(\mathbf{x}_A, \mathbf{x}_R, t) * s(t)$ resides in the region $t < t_d^\epsilon(\mathbf{x}_A, \mathbf{x}_R)$, i.e., above the red dashed line in Fig. 12(b). In other words, the red dashed line in Fig. 12(b) separates the Green's function $G(\mathbf{x}_R, \mathbf{x}_A, t) * s(t)$ from the coda of the time-reversed focusing function $f_2(\mathbf{x}_A, \mathbf{x}_R, -t) * s(t)$. Only the time-reversed direct arrival of the focusing function overlaps the direct arrival of the Green's function (the event directly below the red dashed line in Fig. 12(b)).

Note that this separation between the Green's function and the coda of the focusing function does not hold under all circumstances. For example, in case of strongly scattering media, diffraction curves may cause additional overlap of the Green and focusing functions (Vasconcelos *et al.* 2014, 2015; van der Neut *et al.* 2015b). At large source–receiver offsets, refracted waves in the Green's function may interfere with the focusing function (Wapenaar *et al.* 2014). In elastic media, there is an additional overlap as a result of forward-converted waves (Wapenaar and Slob 2014). In the following, we will assume that the overlap is restricted to the direct arrivals (as in Fig. 12(b)), which is a reasonable assumption in acoustic media with smooth lateral variations, considering limited source–receiver offsets.

We define a window function $w(\mathbf{x}_A, \mathbf{x}_R, t) = H(t_d^\epsilon(\mathbf{x}_A, \mathbf{x}_R) - t)$ (where $H(t)$ is the Heaviside function), which passes the time reversal of the coda of the focusing function and suppresses the entire Green's function. In other words, when applied to Fig. 12(b), this window function passes everything above the red dashed line. We write the focusing function as

$$f_2(\mathbf{x}_A, \mathbf{x}, t) = D(\mathbf{x}_A, \mathbf{x}, t) + M(\mathbf{x}_A, \mathbf{x}, t), \quad (22)$$

where D is the direct arrival of the focusing function and M is the coda (M standing for multiple). Substituting this into equation (20) and applying the window function $w(\mathbf{x}_A, \mathbf{x}_R, t)$ to both sides yields (Wapenaar *et al.* 2013)

$$-M(\mathbf{x}_A, \mathbf{x}_R, -t) = w(\mathbf{x}_A, \mathbf{x}_R, t) \int_{\partial\mathbb{D}_0} d^2\mathbf{x} \int_{-\infty}^t R(\mathbf{x}_R, \mathbf{x}, t - t') \times \{D(\mathbf{x}_A, \mathbf{x}, t') + M(\mathbf{x}_A, \mathbf{x}, t')\} dt'. \quad (23)$$

This is the 3D version of the single-sided 1D Marchenko equation (Marchenko 1955; Burridge 1980; Lamb 1980; Ge 1987; Chadan and Sabatier 1989). Assuming that the reflection response $R(\mathbf{x}_R, \mathbf{x}, t)$ is known from measurements at the upper boundary and assuming that an estimate of the direct arrival $D(\mathbf{x}_A, \mathbf{x}, t)$ of the focusing function is available, this equation can be solved for the coda $M(\mathbf{x}_A, \mathbf{x}, t)$ of the focusing function. This can be done in an iterative way (Wapenaar *et al.* 2014) or by direct inversion (van der Neut *et al.* 2015a). Here, we discuss the iterative method. To this end, we rewrite equation (23) as follows:

$$-M_{k+1}(\mathbf{x}_A, \mathbf{x}_R, -t) = w(\mathbf{x}_A, \mathbf{x}_R, t) \int_{\partial\mathbb{D}_0} d^2\mathbf{x} \int_{-\infty}^t R(\mathbf{x}_R, \mathbf{x}, t - t') \times \{D(\mathbf{x}_A, \mathbf{x}, t') + M_k(\mathbf{x}_A, \mathbf{x}, t')\} dt', \quad (24)$$

with $M_0(\mathbf{x}_A, \mathbf{x}, t) = 0$. The direct arrival $D(\mathbf{x}_A, \mathbf{x}, t)$ is defined as the inverse of the direct arrival of the transmission response between the upper boundary $\partial\mathbb{D}_0$ and the focal plane $\partial\mathbb{D}_A$, but it is often approximated as the time reversal of the direct arrival of the Green's function between these depth levels. Once $M(\mathbf{x}_A, \mathbf{x}, t)$ has been resolved, the focusing function $f_2(\mathbf{x}_A, \mathbf{x}, t)$ follows from equation (22).

Instead of solving equation (20) for the coda of f_2 , which, according to equation (21), consists of a superposition of f_1^+ and the time reversal of $-f_1^-$, one can instead solve equations (18) and (19) for the individual coda's of f_1^+ and f_1^- (Slob *et al.* 2014; Wapenaar *et al.* 2014). To this end, we write these focusing functions as

$$f_1^+(\mathbf{x}, \mathbf{x}_A, t) = D(\mathbf{x}, \mathbf{x}_A, t) + M^+(\mathbf{x}, \mathbf{x}_A, t), \quad (25)$$

$$f_1^-(\mathbf{x}, \mathbf{x}_A, t) = M^-(\mathbf{x}, \mathbf{x}_A, t). \quad (26)$$

Substituting these expressions into equations (18) and (19), applying the window function $w(\mathbf{x}_A, \mathbf{x}_R, t)$ to both sides of these equations, and rewriting the resulting equations as an iterative scheme, we yield the following equations:

$$M_k^-(\mathbf{x}_R, \mathbf{x}_A, t) = w(\mathbf{x}_A, \mathbf{x}_R, t) \int_{\partial\mathbb{D}_0} d^2\mathbf{x} \int_{-\infty}^t R(\mathbf{x}_R, \mathbf{x}, t - t') \times \{D(\mathbf{x}, \mathbf{x}_A, t') + M_k^+(\mathbf{x}, \mathbf{x}_A, t')\} dt', \quad (27)$$

and

$$M_{k+1}^+(\mathbf{x}_R, \mathbf{x}_A, -t) = w(\mathbf{x}_A, \mathbf{x}_R, t) \int_{\partial\mathbb{D}_0} d^2\mathbf{x} \int_{-\infty}^t R(\mathbf{x}_R, \mathbf{x}, t-t') \times M_k^-(\mathbf{x}, \mathbf{x}_A, -t') dt', \quad (28)$$

with $M_0^+(\mathbf{x}, \mathbf{x}_A, t) = 0$. Once $M^+(\mathbf{x}, \mathbf{x}_A, t)$ and $M^-(\mathbf{x}, \mathbf{x}_A, t)$ have been resolved, the focusing functions $f_1^+(\mathbf{x}, \mathbf{x}_A, t)$ and $f_1^-(\mathbf{x}, \mathbf{x}_A, t)$ follow from equations (25) and (26). The focusing functions that are shown in Fig. 11(b) and (d) were obtained with the latter scheme. To this end, we modelled the reflection response $R(\mathbf{x}_R, \mathbf{x}, t)$ of the model shown in Fig. 1(a) in Part I for 600 sources and 600 receivers at the upper boundary, with a horizontal spacing of 10 m. We used a Ricker wavelet with a central frequency of 30 Hz. The direct arrival $D(\mathbf{x}, \mathbf{x}_A, t)$ was modelled in the same medium, for $\mathbf{x}_A = (0, 800)$ m, and for \mathbf{x} at the 600 source positions at the upper boundary. The focusing functions were obtained after seven iterations of equations (27) and (28).

In practice, there are many factors that complicate the retrieval of the focusing functions (van der Neut *et al.* 2015c; Ravasi *et al.* 2016). The measured reflection response contains surface-related multiples and a source wavelet. These surface-related multiples must be eliminated and the response must be deconvolved for the source wavelet to obtain the impulsive reflection response $R(\mathbf{x}_R, \mathbf{x}, t)$. Both tasks, in principle, are accomplished by surface-related multiple elimination (Verschuur, Berkhout and Wapenaar 1992; Dragoset *et al.* 2010; van Groenestijn and Verschuur 2010); however, in practice, amplitude and phase errors and remnants of surface-related multiples may still be present in $R(\mathbf{x}_R, \mathbf{x}, t)$. Anelastic losses form another complicating factor. Slob (2016) discusses a method that accounts for anelastic losses under the assumption that the medium is accessible from two sides. When the medium is accessible from one side only, a time-dependent gain can be applied to the reflection response to compensate for the losses. This assumes that the loss factor is known and constant throughout the medium. These complications can be partly addressed by making the scheme adaptive (van der Neut *et al.* 2015c). Noise, finite acquisition arrays, missing small offsets, and imperfect spatial sampling (particularly in 3D) are other complicating issues. The implementation of the retrieval of the focusing functions for practical situations is the subject of current research.

Data-driven source and receiver redatuming

Once the focusing functions are found, they can be used in equations (18) and (19) to obtain the decomposed Green's

functions $G^-(\mathbf{x}_A, \mathbf{x}_R, t)$ and $G^+(\mathbf{x}_A, \mathbf{x}_R, t)$ or in equation (20) to obtain the Green's function $G(\mathbf{x}_R, \mathbf{x}_A, t)$. We discuss equation (20) in more detail. We can interpret the right-hand side of this expression in two different ways. In an earlier section, we interpreted the focusing function $f_2(\mathbf{x}_A, \mathbf{x}, t)$ at the right-hand side as a downgoing incident field at $\partial\mathbb{D}_0$ (Fig. 12(a)). In this interpretation, the integral in equation (20) evaluates the reflection response to this incident field. The left-hand side states that this reflection response consists of the time-reversed focusing function $-f_2(\mathbf{x}_A, \mathbf{x}_R, -t)$ and the Green's function $G(\mathbf{x}_R, \mathbf{x}_A, t)$, i.e., the response to a virtual source at \mathbf{x}_A , observed by a receiver at \mathbf{x}_R , just above the boundary $\partial\mathbb{D}_0$ (Fig. 12(b)).

Instead of interpreting the right-hand side of equation (20) as an operator R acting on f_2 , we can alternatively interpret it as an operator f_2 acting on R . For the sake of discussion, we slightly reformulate equation (20) and transform it to the frequency (ω) domain using the temporal Fourier transform defined by equation (A-13) in Part I. This gives

$$G(\mathbf{x}_R, \mathbf{x}_A, \omega) = \int_{\partial\mathbb{D}_0} R(\mathbf{x}_R, \mathbf{x}_S, \omega) f_2(\mathbf{x}_A, \mathbf{x}_S, \omega) d^2\mathbf{x}_S + \{f_2(\mathbf{x}_A, \mathbf{x}_R, \omega)\}^*, \quad (29)$$

in which we replaced \mathbf{x} by \mathbf{x}_S to express that this is the source coordinate of the reflection response $R(\mathbf{x}_R, \mathbf{x}_S, \omega)$. Superscript $*$ denotes complex conjugation. The focusing function $f_2(\mathbf{x}_A, \mathbf{x}_S, \omega)$ acts as an operator that redatums the sources of the reflection response $R(\mathbf{x}_R, \mathbf{x}_S, \omega)$ from \mathbf{x}_S at the boundary $\partial\mathbb{D}_0$ to a virtual-source position \mathbf{x}_A in the subsurface. By adding the complex conjugate of the focusing function to the result, we obtain the virtual-source response $G(\mathbf{x}_R, \mathbf{x}_A, \omega)$.

Receiver redatuming can be carried out in a similar way. For this, we need a slightly different representation because the input for receiver redatuming is $G(\mathbf{x}_R, \mathbf{x}_A, \omega)$, with its source in the subsurface (unlike the input $R(\mathbf{x}_R, \mathbf{x}_S, \omega)$ for source redatuming, which has its source and receiver both at the surface). To this end, consider equation (A-27) in the Appendix, interchange \mathbf{x}_A with \mathbf{x}_B , and replace \mathbf{x} at $\partial\mathbb{D}_0$ by \mathbf{x}_R at $\partial\mathbb{D}'_0$ (which is situated just above $\partial\mathbb{D}_0$), hence

$$G_h(\mathbf{x}_B, \mathbf{x}_A, \omega) = -\Im \int_{\partial\mathbb{D}'_0} \frac{4}{\omega\rho(\mathbf{x}_R)} \{\partial_{3,R} f_2(\mathbf{x}_B, \mathbf{x}_R, \omega)\} \times G(\mathbf{x}_R, \mathbf{x}_A, \omega) d^2\mathbf{x}_R, \quad (30)$$

where \Im denotes the imaginary part and $\partial_{3,R}$ stands for differentiation with respect to $x_{3,R}$. Here, the focusing function $\partial_{3,R} f_2(\mathbf{x}_B, \mathbf{x}_R, \omega)$ acts as an operator that redatums the receivers of the Green's function, i.e., $G(\mathbf{x}_R, \mathbf{x}_A, \omega)$, from \mathbf{x}_R

at the boundary $\partial\mathbb{D}'_0$ to a virtual-receiver position \mathbf{x}_B in the subsurface. Note that $\partial_{3,R} f_2(\mathbf{x}_B, \mathbf{x}_R, \omega)$ can be obtained from $f_2(\mathbf{x}_B, \mathbf{x}_R, \omega)$ via equation (A-29). The redatuming result is $G_h(\mathbf{x}_B, \mathbf{x}_A, \omega)$, i.e., the homogeneous Green's function between a virtual source at \mathbf{x}_A and a virtual receiver at \mathbf{x}_B in the subsurface. It is defined as

$$\begin{aligned} G_h(\mathbf{x}_B, \mathbf{x}_A, \omega) &= G(\mathbf{x}_B, \mathbf{x}_A, \omega) + G^*(\mathbf{x}_B, \mathbf{x}_A, \omega) \\ &= 2\Re\{G(\mathbf{x}_B, \mathbf{x}_A, \omega)\}, \end{aligned} \quad (31)$$

where \Re denotes the real part.

The two redatuming steps can be captured by one equation by substituting equation (29) into equation (30); hence

$$\begin{aligned} G_h(\mathbf{x}_B, \mathbf{x}_A, \omega) &= -\Im \int_{\partial\mathbb{D}'_0} \int_{\partial\mathbb{D}_0} \frac{4}{\omega\rho(\mathbf{x}_R)} \{\partial_{3,R} f_2(\mathbf{x}_B, \mathbf{x}_R, \omega)\} \\ &\quad \times R(\mathbf{x}_R, \mathbf{x}_S, \omega) f_2(\mathbf{x}_A, \mathbf{x}_S, \omega) d^2\mathbf{x}_S d^2\mathbf{x}_R \\ &= -\Im \int_{\partial\mathbb{D}'_0} \frac{4}{\omega\rho(\mathbf{x}_R)} \{\partial_{3,R} f_2(\mathbf{x}_B, \mathbf{x}_R, \omega)\} \\ &\quad \times \{f_2(\mathbf{x}_A, \mathbf{x}_R, \omega)\}^* d^2\mathbf{x}_R. \end{aligned} \quad (32)$$

The double integral has the same form as standard primary redatuming schemes (Berkhout 1982; Berryhill 1984), but equation (32) takes multiple scattering into account. The double integral can also be seen as an alternative for source–receiver interferometry, which also takes multiple scattering into account (Halliday and Curtis 2010). However, whereas source–receiver interferometry is formulated in terms of closed boundary integrals, equation (32) contains open boundary integrals only.

We apply equation (32) to the Fourier transform of the modelled reflection response $R(\mathbf{x}_R, \mathbf{x}_S, t)$ of the medium shown in Fig. 1 of Part I. First, the focusing functions are retrieved from this reflection response using the iterative scheme described by equations (27) and (28) for fixed $\mathbf{x}_A = (0, 800)$ m and variable \mathbf{x}_B . Applying these focusing functions to the reflection response, as described by equation (32), and transforming the result back from the frequency domain to the time domain gives the homogeneous Green's function $G_h(\mathbf{x}_B, \mathbf{x}_A, t)$ for fixed \mathbf{x}_A and variable \mathbf{x}_B , as a function of time t . Figure 15 shows snapshots of this homogeneous Green's function for $t = 0.004$ seconds, $t = 0.15$ seconds, and $t = 0.30$ seconds. Note the similarity with Fig. 14. However, whereas Fig. 14 was obtained by emitting a focusing function from the upper boundary into the known medium (and adding to this its time reversal), Fig. 15 was obtained from the reflection response at the upper boundary and the direct arrivals between all subsurface points and the upper boundary. In this example, the

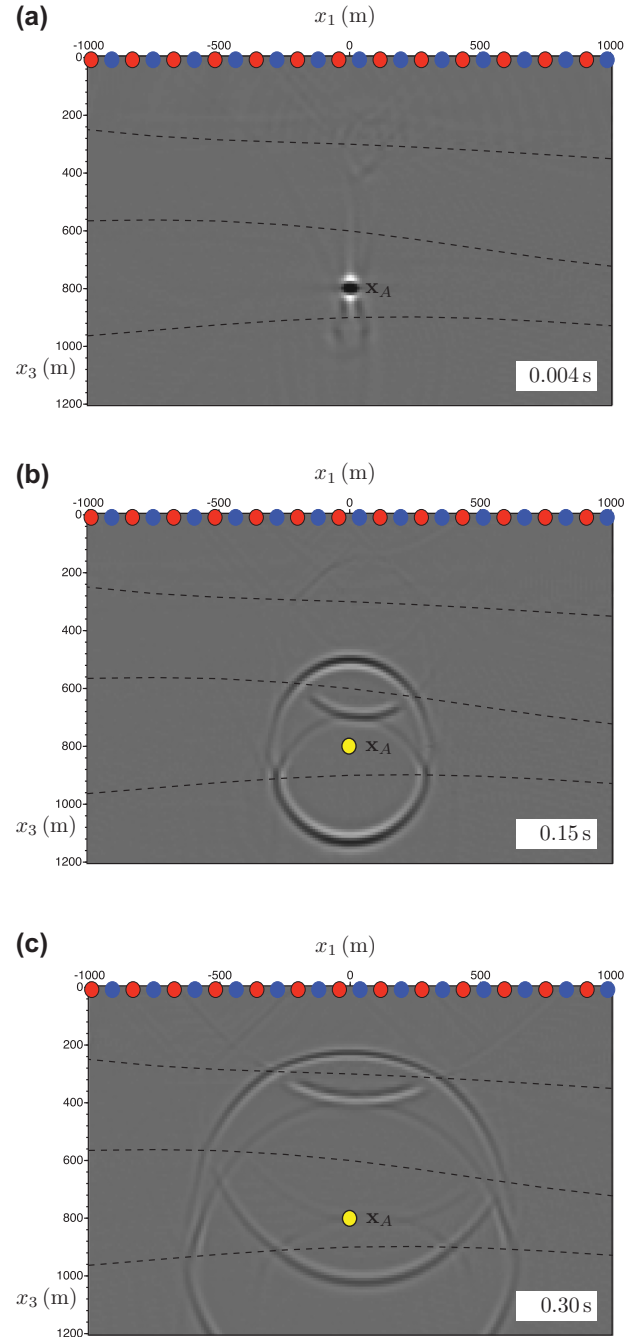


Figure 15 Homogeneous Green's function $G_h(\mathbf{x}_B, \mathbf{x}_A, t)$, retrieved from reflection response at the upper boundary.

direct arrivals were modelled in the true medium. In practice, they will be modelled in a macro velocity model, meaning that the travel times and amplitudes will not be exact. This will of course affect the quality of the virtual source and hence the accuracy of the wavefront shapes and amplitudes of the retrieved homogeneous Green's function. Errors will be in the

same order as those in the direct arrivals. However, we want to emphasise that the treatment of multiple reflections is stable with respect to errors in the direct arrivals. This is because the internal multiples in the retrieved homogeneous Green's function $G_h(\mathbf{x}_B, \mathbf{x}_A, t)$ come directly from the reflection response $R(\mathbf{x}_R, \mathbf{x}_S, t)$, without the need to estimate the reflecting boundaries in an intermediate step. Current research concerns data-driven estimation of the amplitudes of the direct arrivals and hence of the homogeneous Green's function (Brackenhoff 2016).

TWO HOMOGENEOUS GREEN'S FUNCTION REPRESENTATIONS

We started Part I of this paper with a review of time-reversal acoustics, which is essentially based on the following representation of the homogeneous Green's function (Oristaglio 1989; Porter 1970)

$$G_h(\mathbf{x}_B, \mathbf{x}_A, \omega) = \oint_{\partial\mathbb{D}} \frac{-1}{j\omega\rho(\mathbf{x})} \left\{ \partial_i G(\mathbf{x}_B, \mathbf{x}, \omega) G^*(\mathbf{x}, \mathbf{x}_A, \omega) - G(\mathbf{x}_B, \mathbf{x}, \omega) \partial_i G^*(\mathbf{x}, \mathbf{x}_A, \omega) \right\} n_i d^2\mathbf{x} \quad (33)$$

(Part I, Appendix A, equation (A-20)), where $\partial\mathbb{D}$ is a closed boundary, enclosing \mathbf{x}_A and \mathbf{x}_B .

Equation (30) is a simplified version of the following single-sided representation of the homogeneous Green's function:

$$G_h(\mathbf{x}_B, \mathbf{x}_A, \omega) = \int_{\partial\mathbb{D}_0} \frac{2}{\omega\rho(\mathbf{x})} (\partial_3 G_h(\mathbf{x}_B, \mathbf{x}, \omega) \Im\{f_1(\mathbf{x}, \mathbf{x}_A, \omega)\} - G_h(\mathbf{x}_B, \mathbf{x}, \omega) \Im\{\partial_3 f_1(\mathbf{x}, \mathbf{x}_A, \omega)\}) d^2\mathbf{x} \quad (34)$$

(Part II, Appendix, equation (A-21)), where $\partial\mathbb{D}_0$ is a horizontal open boundary, above \mathbf{x}_A and \mathbf{x}_B . The underlying assumption for equation (30) is that the medium at and above $\partial\mathbb{D}_0$ is homogeneous. Equation (34) also holds when the actual medium at and above $\partial\mathbb{D}_0$ is inhomogeneous.

Equations (33) and (34) have a similar structure and accomplish the same task, namely, retrieving the response to an isotropic virtual source at \mathbf{x}_A , observed by a receiver at \mathbf{x}_B . Since the left-hand sides of both expressions are the same, the associated virtual-source functions are the same; they have been extensively discussed in Part I. In the classical homogeneous Green's function representation, i.e., equation (33), a time-reversed Green's function (which, in the frequency domain, is represented by the complex-conjugated Green's function) is emitted from the enclosing boundary $\partial\mathbb{D}$ into the medium. In the single-sided homogeneous Green's function representation, i.e., equation (34), a focusing function is

emitted from the open boundary $\partial\mathbb{D}_0$ into the medium. The different character of time-reversed Green's functions and focusing functions has been illustrated, for the 1D case, in Fig. 6(c) and (f).

In the previous section, we have discussed redatuming, accounting for multiple reflections, as an application of the single-sided homogeneous Green's function representation. Based on the analogy with the classical representation, other applications of the single-sided representation come to mind, such as holographic imaging, inverse scattering, time-reversal acoustics, source imaging, and interferometric Green's function retrieval. In these methodologies, the medium is often accessible from one side only; hence, the single-sided homogeneous Green's function representation, i.e., equation (34), forms an attractive starting point for improving these methodologies.


CONCLUSIONS

By approaching focusing as an inverse filtering process rather than a time-reversal process, we have derived a focusing function suited for single-sided focusing in 2D and 3D inhomogeneous lossless media. The focal spot at $t = 0$, obtained with this focusing function, acts as an isotropic virtual source for the field at $t > 0$, similar to the virtual source obtained by emitting a time-reversed point-source response from a closed boundary into the medium (as discussed in Part I). The focusing function can be retrieved from the single-sided reflection response and an estimate of the direct arrivals between the focal point and the surface. A macro velocity model of the medium suffices to define these direct arrivals. Hence, the single-sided focusing approach needs the same input as standard seismic redatuming or imaging. However, unlike these standard methods, the discussed single-sided focusing approach yields the full response (including correct multiple scattering) between virtual sources and virtual receivers anywhere in the subsurface. This forms the ideal starting point for improved holographic imaging, time-reversal acoustics, seismic interferometry etc., for situations in which multiple scattering plays a significant role and the medium of interest is accessible from one side only.

ACKNOWLEDGEMENTS

The authors would like to thank Matteo Ravasi, an anonymous reviewer, and associate editor Colin Thomson for their constructive comments, which helped us improve the paper.

ORCID

Kees Wapenaar  <http://orcid.org/0000-0002-1620-8282>

REFERENCES

- Aki K. and Richards P.G. 1980. *Quantitative Seismology*, Vol. I. San Francisco, CA: W.H. Freeman and Company.
- Anstey N.A. and O'Doherty R.F. 1971. Reflections on amplitudes. *Geophysical Prospecting* **19**, 430–458.
- Becker T., Elison P., van Manen D.-J., Donahue C., Greenhalgh S., Brogini F. and Robertsson J.O.A. 2016. Experimental Marchenko focusing in a variable diameter sound wave tube. 86th SEG annual international meeting, Expanded Abstracts, 5144–5148.
- Berkhout A.J. 1974. Related properties of minimum-phase and zero-phase time functions. *Geophysical Prospecting* **22**(4), 683–709.
- Berkhout A.J. 1982. *Seismic Migration. Imaging of Acoustic Energy by Wave Field Extrapolation. A. Theoretical Aspects*. Elsevier.
- Berkhout A.J. and van Wulfften Palthe D.W. 1979. Migration in terms of spatial deconvolution. *Geophysical Prospecting* **27**(1), 261–291.
- Berryhill J.R. 1984. Wave-equation datuming before stack. *Geophysics* **49**, 2064–2066.
- Brackenhoff J. 2016. *Rescaling of incorrect source strength using Marchenko redatuming*. MSc thesis, Delft University of Technology, The Netherlands.
- Brogini F. and Snieder R. 2012. Connection of scattering principles: a visual and mathematical tour. *European Journal of Physics* **33**, 593–613.
- Burrige R. 1980. The Gelfand-Levitan, the Marchenko, and the Gopinath-Sondhi integral equations of inverse scattering theory, regarded in the context of inverse impulse-response problems. *Wave Motion* **2**, 305–323.
- Chadan K. and Sabatier P.C. 1989. *Inverse Problems in Quantum Scattering Theory*. Berlin, Germany: Springer.
- Dragoset B., Verschuur E., Moore I. and Bisley R. 2010. A perspective on 3D surface-related multiple elimination. *Geophysics* **75**, 75A245–75A261.
- Fokkema J.T. and van den Berg P.M. 1993. *Seismic Applications of Acoustic Reciprocity*. Amsterdam, The Netherlands: Elsevier.
- Ge D.B. 1987. An iterative technique in one-dimensional profile inversion. *Inverse Problems* **3**, 399–406.
- Halliday D. and Curtis A. 2010. An interferometric theory of source-receiver scattering and imaging. *Geophysics* **75**(6), SA95–SA103.
- Lamb G.L. 1980. *Elements of Soliton Theory*. New York, NY: John Wiley and Sons, Inc.
- Marchenko V.A. 1955. Reconstruction of the potential energy from the phases of the scattered waves (in Russian). *Doklady Akademii Nauk SSSR* **104**(5), 695–698.
- Oristaglio M.L. 1989. An inverse scattering formula that uses all the data. *Inverse Problems* **5**, 1097–1105.
- Porter R.P. 1970. Diffraction-limited, scalar image formation with holograms of arbitrary shape. *Journal of the Optical Society of America* **60**, 1051–1059.
- Ravasi M., Vasconcelos I., Kritski A., Curtis A., da Costa Filho C.A. and Meles G.A. 2016. Target-oriented Marchenko imaging of a North Sea field. *Geophysical Journal International* **205**, 99–104.
- Robinson E.A. 1954. *Predictive decomposition of seismic traces with applications to seismic exploration*. PhD thesis, Massachusetts Institute of Technology, USA.
- Robinson E.A. and Treitel S. 1976. Net downgoing energy and the resulting minimum-phase property of downgoing waves. *Geophysics* **41**(6), 1394–1396.
- Rose J.H. 2001. “Single-sided” focusing of the time-dependent Schrödinger equation. *Physical Review A* **65**, 012707.
- Rose J.H. 2002. ‘Single-sided’ autofocusing of sound in layered materials. *Inverse Problems* **18**, 1923–1934.
- Singh S., Snieder R., van der Neut J., Thorbecke J., Slob E. and Wapenaar K. 2017. Accounting for free-surface multiples in Marchenko imaging. *Geophysics* **82**(1), R19–R30.
- Slob E., Wapenaar K., Brogini F. and Snieder R. 2014. Seismic reflector imaging using internal multiples with Marchenko-type equations. *Geophysics* **79**(2), S63–S76.
- Slob E. 2016. Green’s function retrieval and Marchenko imaging in a dissipative acoustic medium. *Physical Review Letters* **116**, 164301.
- Snieder R., Sheiman J. and Calvert R. 2006. Equivalence of the virtual-source method and wave-field deconvolution in seismic interferometry. *Physical Review E* **73**, 066620.
- Tanter M., Thomas J.-L. and Fink M. 2000. Time-reversal and the inverse filter. *Journal of the Acoustical Society of America* **108**(1), 223–234.
- Thomson C.J., Kitchenside P.W. and Fletcher R.P. 2016. Theory of reflectivity blurring in seismic depth imaging. *Geophysical Journal International* **205**, 837–855.
- Treitel S. and Robinson E.A. 1964. The stability of digital filters. *IEEE Transactions on Geoscience Electronics* **2**(1), 6–18.
- van der Neut J., Thorbecke J., Wapenaar K. and Slob E. 2015a. Inversion of the multidimensional Marchenko equation. 77th EAGE annual international meeting, Extended Abstracts, We-N106-04.
- van der Neut J., Vasconcelos I. and Wapenaar K. 2015b. On Green’s function retrieval by iterative substitution of the coupled Marchenko equations. *Geophysical Journal International* **203**, 792–813.
- van der Neut J., Wapenaar K., Thorbecke J., Slob E. and Vasconcelos I. 2015c. An illustration of adaptive Marchenko imaging. *The Leading Edge* **34**, 818–822.
- van Groenestijn G.J.A. and Verschuur D.J. 2010. Estimation of primaries by sparse inversion from passive seismic data. *Geophysics* **75**(4), SA61–SA69.
- Vasconcelos I., van Manen D.-J., Ravasi M., Wapenaar K. and van der Neut J. 2014. Marchenko redatuming: advantages and limitations in complex media. 84th SEG annual international meeting, Workshop W-11: Using Multiples as Signal for Imaging.
- Vasconcelos I., Wapenaar K., van der Neut J., Thomson C. and Ravasi M. 2015. Using inverse transmission matrices for Marchenko redatuming in highly complex media. 85th SEG annual international meeting, Expanded Abstracts, 5081–5086.
- Verschuur D.J., Berkhout A.J. and Wapenaar C.P.A. 1992. Adaptive surface-related multiple elimination. *Geophysics* **57**(9), 1166–1177.
- Wapenaar C.P.A. 1993. Kirchhoff-Helmholtz downward extrapolation in a layered medium with curved interfaces. *Geophysical Journal International* **115**, 445–455.

- Wapenaar C.P.A. and Berkhout A.J. 1989. *Elastic wave field extrapolation*. Amsterdam, The Netherlands: Elsevier.
- Wapenaar K. and Slob E. 2014. On the Marchenko equation for multicomponent single-sided reflection data. *Geophysical Journal International* **199**, 1367–1371.
- Wapenaar K., van der Neut J. and Ruigrok E. 2008. Passive seismic interferometry by multidimensional deconvolution. *Geophysics* **73**(6), A51–A56.
- Wapenaar K., Brogini F., Slob E. and Snieder R. 2013. Three-dimensional single-sided Marchenko inverse scattering, data-driven focusing, Green's function retrieval, and their mutual relations. *Physical Review Letters* **110**, 084301.
- Wapenaar K., Thorbecke J., van der Neut J., Brogini F., Slob E. and Snieder R. 2014. Marchenko imaging. *Geophysics* **79**(3), WA39–WA57.
- Wapenaar K., Thorbecke J. and van der Neut J. 2016. A single-sided homogeneous Green's function representation for holographic imaging, inverse scattering, time-reversal acoustics and interferometric Green's function retrieval. *Geophysical Journal International* **205**, 531–535.

APPENDIX A: SINGLE-SIDED GREEN'S FUNCTION REPRESENTATIONS

Reciprocity theorems

The starting point for the derivation of the single-sided Green's function representations is formed by the reciprocity theorems of the convolution type and of the correlation type, both in the frequency (ω) domain. These theorems have been introduced in Appendix A of Part I. Here, we reformulate them by substituting $v_i = -(j\omega\rho)^{-1}\partial_i p$. Hence, these theorems become

$$\begin{aligned} & \int_{\mathbb{D}} \{p_A q_B - q_A p_B\} d^3 \mathbf{x} \\ &= - \oint_{\partial \mathbb{D}} \frac{1}{j\omega\rho} \{p_A \partial_i p_B - (\partial_i p_A) p_B\} n_i d^2 \mathbf{x} \end{aligned} \quad (\text{A-1})$$

and

$$\begin{aligned} & \int_{\mathbb{D}} \{p_A^* q_B + q_A^* p_B\} d^3 \mathbf{x} \\ &= - \oint_{\partial \mathbb{D}} \frac{1}{j\omega\rho} \{p_A^* \partial_i p_B - (\partial_i p_A^*) p_B\} n_i d^2 \mathbf{x}, \end{aligned} \quad (\text{A-2})$$

respectively. Here, $p = p(\mathbf{x}, \omega)$ is the acoustic pressure, $q = q(\mathbf{x}, \omega)$ is a source distribution of volume injection rate density, and $\rho = \rho(\mathbf{x})$ is the mass density. Subscripts A and B denote two independent acoustic states. \mathbb{D} is an arbitrary spatial domain, enclosed by boundary $\partial \mathbb{D}$ with outward pointing normal $\mathbf{n} = (n_1, n_2, n_3)$. The medium, which is assumed to be lossless, is the same in both states inside $\partial \mathbb{D}$. Outside $\partial \mathbb{D}$, the medium parameters may be different in the two states.

For the derivation of the single-sided Green's function representations, we redefine \mathbb{D} as the domain enclosed by two horizontal boundaries $\partial \mathbb{D}_0$ and $\partial \mathbb{D}_A$ and a cylindrical boundary $\partial \mathbb{D}_{\text{cyl}}$. Here, $\partial \mathbb{D}_0$ is the accessible boundary of the medium where the measurements take place. For simplicity, we will assume that is a horizontal boundary defined by $x_3 = x_{3,0}$. Furthermore, $\partial \mathbb{D}_A$ is a horizontal boundary at the depth of \mathbf{x}_A ; hence, it is defined by $x_3 = x_{3,A}$. Finally, $\partial \mathbb{D}_{\text{cyl}}$ is a cylindrical boundary with a vertical axis through \mathbf{x}_A and infinite radius. This cylindrical boundary exists between $\partial \mathbb{D}_0$ and $\partial \mathbb{D}_A$ and closes the boundary $\partial \mathbb{D}$. In the next sections, we substitute focusing functions for state A and Green's functions for state B . The contribution of the boundary integral over $\partial \mathbb{D}_{\text{cyl}}$ in equations (A-1) and (A-2) thus vanishes but for another reason than Sommerfeld's radiation condition. The argumentation is as follows (Wapenaar and Berkhout 1989). The integrand contains products of functions, in which each decay with $1/r$ for $r \rightarrow \infty$, where r is the distance from \mathbf{x}_A ; hence, the integrand decays with $1/r^2$ for $r \rightarrow \infty$. The surface area of the cylindrical boundary is proportional to r ; hence, the integral decays with $1/r$ for $r \rightarrow \infty$ and thus vanishes. This implies that we can restrict the integration to the boundaries $\partial \mathbb{D}_0$ and $\partial \mathbb{D}_A$. Note that $\mathbf{n} = (0, 0, -1)$ on $\partial \mathbb{D}_0$ and $\mathbf{n} = (0, 0, +1)$ on $\partial \mathbb{D}_A$.

Single-sided representations of the Green's functions between the surface and \mathbf{x}_A

We derive equations (18) and (19), which are the single-sided representations of the Green's functions between \mathbf{x}_R at the surface and \mathbf{x}_A in the subsurface. We assume that the medium at and above $\partial \mathbb{D}_0$ is homogeneous. A similar derivation for the situation in which $\partial \mathbb{D}_0$ is a free surface is presented by Singh *et al.* (2017). For state B , we consider the Fourier transform of the Green's function introduced in equation (12); hence, $G(\mathbf{x}, \mathbf{x}_R, \omega) = G^+(\mathbf{x}, \mathbf{x}_R, \omega) + G^-(\mathbf{x}, \mathbf{x}_R, \omega)$, with \mathbf{x}_R defined just above $\partial \mathbb{D}_0$, i.e., $\mathbf{x}_R = (\mathbf{x}_{H,R}, x_{3,0} - \epsilon)$. $G(\mathbf{x}, \mathbf{x}_R, \omega)$ obeys the temporal Fourier transform of wave equation (A-5) in Appendix A in Part I. We define the spatial Fourier transform of $G(\mathbf{x}, \mathbf{x}_R, \omega)$ as $\tilde{G}(\mathbf{k}_H, x_3, \mathbf{x}_R, \omega) = \int_{-\infty}^{\infty} \int_{-\infty}^{\infty} G(\mathbf{x}_H, x_3, \mathbf{x}_R, \omega) \exp\{j\mathbf{k}_H \cdot \mathbf{x}_H\} d^2 \mathbf{x}_H$, with $\mathbf{k}_H = (k_1, k_2)$. For finite ϵ , the downgoing part of this Green's function below \mathbf{x}_R and above $\partial \mathbb{D}_0$ reads in the wavenumber-frequency (\mathbf{k}_H, ω) domain (Aki and Richards 1980; Fokkema and van den Berg 1993)

$$\begin{aligned} \tilde{G}^+(\mathbf{k}_H, x_3, \mathbf{x}_R, \omega) &= j\omega\rho \exp\{j\mathbf{k}_H \cdot \mathbf{x}_{H,R}\} \\ &\times \frac{\exp\{-jk_3(x_3 - (x_{3,0} - \epsilon))\}}{2jk_3}, \end{aligned} \quad (\text{A-3})$$

where $k_3 = \sqrt{\omega^2/c^2 - \mathbf{k}_H \cdot \mathbf{k}_H}$ and with ρ and c being the mass density and propagation velocity of the homogeneous upper half-space. Note that $\partial_3 \tilde{G}^+ = -jk_3 \tilde{G}^+$; hence

$$\begin{aligned} & [\partial_3 \tilde{G}^+(\mathbf{k}_H, x_3, \mathbf{x}_R, \omega)]_{x_3=x_{3,0}} \\ &= -\frac{1}{2} j\omega\rho \exp\{j\mathbf{k}_H \cdot \mathbf{x}_{H,R}\} \exp\{-jk_3\epsilon\}. \end{aligned} \quad (\text{A-4})$$

Taking $\epsilon \rightarrow 0$ and transforming the result back to the space-frequency domain gives

$$[\partial_3 G^+(\mathbf{x}, \mathbf{x}_R, \omega)]_{x_3=x_{3,0}} = -\frac{1}{2} j\omega\rho(\mathbf{x}_R)\delta(\mathbf{x}_H - \mathbf{x}_{H,R}). \quad (\text{A-5})$$

The inverse temporal Fourier transform of this expression gives equation (13).

We relate the upgoing part of the Green's function at $\partial\mathbb{D}_0$ to the reflection response $R(\mathbf{x}_R, \mathbf{x}, \omega)$ of the inhomogeneous medium below $\partial\mathbb{D}_0$ as follows:

$$[\partial_3 G^-(\mathbf{x}, \mathbf{x}_R, \omega)]_{x_3=x_{3,0}} = \left[\frac{1}{2} j\omega\rho(\mathbf{x})R(\mathbf{x}_R, \mathbf{x}, \omega) \right]_{x_3=x_{3,0}}. \quad (\text{A-6})$$

The inverse temporal Fourier transform of this expression gives equation (14).

For state A , we consider the temporal Fourier transform of the focusing function introduced in equation (15); hence, $f_1(\mathbf{x}, \mathbf{x}_A, \omega) = f_1^+(\mathbf{x}, \mathbf{x}_A, \omega) + f_1^-(\mathbf{x}, \mathbf{x}_A, \omega)$. Recall that this focusing function is defined in a source-free truncated medium, which is identical to the actual medium above the focal plane $\partial\mathbb{D}_A$ but homogeneous below this plane. The focusing conditions at the focal plane are the Fourier transforms of equations (16) and (17); hence

$$[\partial_3 f_1^+(\mathbf{x}, \mathbf{x}_A, \omega)]_{x_3=x_{3,A}} = -\frac{1}{2} j\omega\rho(\mathbf{x}_A)\delta(\mathbf{x}_H - \mathbf{x}_{H,A}), \quad (\text{A-7})$$

$$[\partial_3 f_1^-(\mathbf{x}, \mathbf{x}_A, \omega)]_{x_3=x_{3,A}} = 0. \quad (\text{A-8})$$

With these choices, the domain \mathbb{D} is source free in both states (the focusing functions have no sources, and the source of the Green's function is chosen just above $\partial\mathbb{D}_0$, i.e., outside \mathbb{D}). Hence, we can set the left-hand sides of equations (A-1) and (A-2) to be equal to zero. As discussed earlier, the boundary integrals on the right-hand sides are taken along the boundary $\partial\mathbb{D} = \partial\mathbb{D}_0 \cup \partial\mathbb{D}_A$, with $n_3 = -1$ on $\partial\mathbb{D}_0$ and $n_3 = +1$ on $\partial\mathbb{D}_A$. Equations (A-5)–(A-8) define conditions for downgoing and upgoing waves at $\partial\mathbb{D}_0$ and $\partial\mathbb{D}_A$; hence, we need to apply decomposition to the fields at the right-hand sides of equations (A-1) and (A-2). More specifically, equations (A-5) and (A-6) define conditions for the derivative of the field in state B at $\partial\mathbb{D}_0$, whereas equations (A-7) and (A-8) are conditions for the derivative of the field in state A at $\partial\mathbb{D}_A$. Taking all these

into account, following a similar derivation as in Appendix B in Wapenaar and Berkhout (1989), we reformulate equations (A-1) and (A-2) as

$$\begin{aligned} 0 &= \int_{\partial\mathbb{D}_0} \frac{2}{j\omega\rho} \{p_A^+ \partial_3 p_B^- + p_A^- \partial_3 p_B^+\} d^2\mathbf{x} \\ &+ \int_{\partial\mathbb{D}_A} \frac{2}{j\omega\rho} \{(\partial_3 p_A^+) p_B^- + (\partial_3 p_A^-) p_B^+\} d^2\mathbf{x}, \end{aligned} \quad (\text{A-9})$$

$$\begin{aligned} 0 &= \int_{\partial\mathbb{D}_0} \frac{2}{j\omega\rho} \{(p_A^+)^* \partial_3 p_B^+ + (p_A^-)^* \partial_3 p_B^-\} d^2\mathbf{x} \\ &+ \int_{\partial\mathbb{D}_A} \frac{2}{j\omega\rho} \{(\partial_3 p_A^+)^* p_B^+ + (\partial_3 p_A^-)^* p_B^-\} d^2\mathbf{x}. \end{aligned} \quad (\text{A-10})$$

The downgoing and upgoing fields are pressure normalised; hence, $p_A^+ + p_A^- = p_A$ and $p_B^+ + p_B^- = p_B$. Equation (A-9) is exact, whereas in equation (A-10), evanescent wave components on $\partial\mathbb{D}_0$ and $\partial\mathbb{D}_A$ are neglected. Substituting $p_A^\pm(\mathbf{x}, \omega) = f_1^\pm(\mathbf{x}, \mathbf{x}_A, \omega)$ and $p_B^\pm(\mathbf{x}, \omega) = G^\pm(\mathbf{x}, \mathbf{x}_R, \omega)$ into equations (A-9) and (A-10), using conditions (A-5)–(A-8), we obtain

$$\begin{aligned} & G^-(\mathbf{x}_A, \mathbf{x}_R, \omega) + f_1^-(\mathbf{x}_R, \mathbf{x}_A, \omega) \\ &= \int_{\partial\mathbb{D}_0} R(\mathbf{x}_R, \mathbf{x}, \omega) f_1^+(\mathbf{x}, \mathbf{x}_A, \omega) d^2\mathbf{x} \end{aligned} \quad (\text{A-11})$$

and

$$\begin{aligned} & G^+(\mathbf{x}_A, \mathbf{x}_R, \omega) - \{f_1^+(\mathbf{x}_R, \mathbf{x}_A, \omega)\}^* \\ &= - \int_{\partial\mathbb{D}_0} R(\mathbf{x}_R, \mathbf{x}, \omega) \{f_1^-(\mathbf{x}, \mathbf{x}_A, \omega)\}^* d^2\mathbf{x}, \end{aligned} \quad (\text{A-12})$$

respectively. Adding these equations and using source-receiver reciprocity for the Green's function gives

$$\begin{aligned} & G(\mathbf{x}_R, \mathbf{x}_A, \omega) - \{f_2(\mathbf{x}_A, \mathbf{x}_R, \omega)\}^* \\ &= \int_{\partial\mathbb{D}_0} R(\mathbf{x}_R, \mathbf{x}, \omega) f_2(\mathbf{x}_A, \mathbf{x}, \omega) d^2\mathbf{x}, \end{aligned} \quad (\text{A-13})$$

with

$$f_2(\mathbf{x}_A, \mathbf{x}, \omega) = f_1^+(\mathbf{x}, \mathbf{x}_A, \omega) - \{f_1^-(\mathbf{x}, \mathbf{x}_A, \omega)\}^*. \quad (\text{A-14})$$

These are the single-sided representations of the Green's functions between \mathbf{x}_R at the surface and \mathbf{x}_A in the subsurface. Applying an inverse temporal Fourier transform to these expressions gives equations (18)–(21).

Single-sided representation of the homogeneous Green's function between \mathbf{x}_A and \mathbf{x}_B

We derive a single-sided representation of the homogeneous Green's function $G_h(\mathbf{x}_B, \mathbf{x}_A, \omega) = G(\mathbf{x}_B, \mathbf{x}_A, \omega) + G^*(\mathbf{x}_B, \mathbf{x}_A, \omega) = 2\Re\{G(\mathbf{x}_B, \mathbf{x}_A, \omega)\}$, where \Re denotes the real

part, with \mathbf{x}_A and \mathbf{x}_B both below $\partial\mathbb{D}_0$. This can be done in different ways. In recent work (Wapenaar, Thorbecke and van der Neut 2016), we have used the classical homogeneous Green's function representation of equation (33) (Porter 1970; Oristaglio 1989) as the starting point. We replaced the closed boundary by two horizontal boundaries (one above and one below \mathbf{x}_A and \mathbf{x}_B) and added an auxiliary function to the Green's function in state A , such that this modified Green's function and its vertical derivative vanished on the lower boundary (Cauchy boundary condition). As a consequence, the integral along the lower boundary vanished. By taking the real part of the remaining integral along the upper boundary, we thus obtained a single-sided homogeneous Green's function representation. Here, we follow a different approach, more in line with the derivation of the single-sided representations of the Green's functions between the surface and \mathbf{x}_A (equations (A-11)–(A-13)). We consider again equations (A-1) and (A-2), with $\partial\mathbb{D} = \partial\mathbb{D}_0 \cup \partial\mathbb{D}_A$, where $\partial\mathbb{D}_A$ is again chosen at the depth of \mathbf{x}_A . For the moment, we will not assume that the actual medium above $\partial\mathbb{D}_0$ is homogeneous (we will make this assumption at a later stage). For state A , we take the same focusing function as in the previous analysis in a truncated medium, which is identical to the actual medium in \mathbb{D} but homogeneous above $\partial\mathbb{D}_0$ and below $\partial\mathbb{D}_A$. The focusing conditions at the focal plane $\partial\mathbb{D}_A$ are again defined by equations (A-7) and (A-8). For state B , we take the Green's function $G(\mathbf{x}, \mathbf{x}_B, \omega) = G^+(\mathbf{x}, \mathbf{x}_B, \omega) + G^-(\mathbf{x}, \mathbf{x}_B, \omega)$. Its source at \mathbf{x}_B may lie above or below $\partial\mathbb{D}_A$. Unlike in the previous analysis, we do not define conditions at $\partial\mathbb{D}_0$. Hence, in equations (A-1) and (A-2), we decompose this time only the fields at the focal plane $\partial\mathbb{D}_A$ to accommodate for the focusing conditions (A-7) and (A-8). Hence

$$\begin{aligned} & \int_{\mathbb{D}} \{p_A q_B - q_A p_B\} d^3 \mathbf{x} \\ &= \int_{\partial\mathbb{D}_0} \frac{1}{j\omega\rho} \{p_A \partial_3 p_B - (\partial_3 p_A) p_B\} d^2 \mathbf{x} \\ &+ \int_{\partial\mathbb{D}_A} \frac{2}{j\omega\rho} \{(\partial_3 p_A^+) p_B^- + (\partial_3 p_A^-) p_B^+\} d^2 \mathbf{x}, \end{aligned} \quad (\text{A-15})$$

$$\begin{aligned} & \int_{\mathbb{D}} \{p_A^* q_B + q_A^* p_B\} d^3 \mathbf{x} \\ &= \int_{\partial\mathbb{D}_0} \frac{1}{j\omega\rho} \{p_A^* \partial_3 p_B - (\partial_3 p_A^*) p_B\} d^2 \mathbf{x} \\ &+ \int_{\partial\mathbb{D}_A} \frac{2}{j\omega\rho} \{(\partial_3 p_A^+)^* p_B^- + (\partial_3 p_A^-)^* p_B^-\} d^2 \mathbf{x}. \end{aligned} \quad (\text{A-16})$$

Equation (A-15) is exact, whereas in equation (A-16), evanescent wave components on $\partial\mathbb{D}_A$ are neglected. Substituting $p_A^\pm(\mathbf{x}, \omega) = f_1^\pm(\mathbf{x}, \mathbf{x}_A, \omega)$, $q_A(\mathbf{x}, \omega) = 0$, $p_B^\pm(\mathbf{x}, \omega) = G^\pm(\mathbf{x}, \mathbf{x}_B, \omega)$, and $q_B(\mathbf{x}, \omega) = \delta(\mathbf{x} - \mathbf{x}_B)$ into equations (A-15) and (A-16), using equations (A-7) and (A-8), gives

$$\begin{aligned} & G^-(\mathbf{x}_A, \mathbf{x}_B, \omega) + H(x_{3,A} - x_{3,B}) f_1(\mathbf{x}_B, \mathbf{x}_A, \omega) \\ &= \int_{\partial\mathbb{D}_0} \frac{1}{j\omega\rho(\mathbf{x})} (f_1(\mathbf{x}, \mathbf{x}_A, \omega) \partial_3 G(\mathbf{x}, \mathbf{x}_B, \omega) \\ &- \{\partial_3 f_1(\mathbf{x}, \mathbf{x}_A, \omega)\} G(\mathbf{x}, \mathbf{x}_B, \omega)) d^2 \mathbf{x} \end{aligned} \quad (\text{A-17})$$

and

$$\begin{aligned} & G^+(\mathbf{x}_A, \mathbf{x}_B, \omega) - H(x_{3,A} - x_{3,B}) f_1^*(\mathbf{x}_B, \mathbf{x}_A, \omega) \\ &= - \int_{\partial\mathbb{D}_0} \frac{1}{j\omega\rho(\mathbf{x})} (f_1^*(\mathbf{x}, \mathbf{x}_A, \omega) \partial_3 G(\mathbf{x}, \mathbf{x}_B, \omega) \\ &- \{\partial_3 f_1^*(\mathbf{x}, \mathbf{x}_A, \omega)\} G(\mathbf{x}, \mathbf{x}_B, \omega)) d^2 \mathbf{x}, \end{aligned} \quad (\text{A-18})$$

respectively, where $H(x_3)$ is the Heaviside function. This Heaviside function is equal to 1 when \mathbf{x}_B lies above $\partial\mathbb{D}_A$ (since, in this case, the singularity of the delta function $\delta(\mathbf{x} - \mathbf{x}_B)$ lies inside \mathbb{D}), whereas it is equal to 0 when \mathbf{x}_B lies below $\partial\mathbb{D}_A$. Summing these two equations yields

$$\begin{aligned} & G(\mathbf{x}_A, \mathbf{x}_B, \omega) + H(x_{3,A} - x_{3,B}) 2j\Im\{f_1(\mathbf{x}_B, \mathbf{x}_A, \omega)\} \\ &= \int_{\partial\mathbb{D}_0} \frac{2}{\omega\rho(\mathbf{x})} (\Im\{f_1(\mathbf{x}, \mathbf{x}_A, \omega)\} \partial_3 G(\mathbf{x}, \mathbf{x}_B, \omega) \\ &- \Im\{\partial_3 f_1(\mathbf{x}, \mathbf{x}_A, \omega)\} G(\mathbf{x}, \mathbf{x}_B, \omega)) d^2 \mathbf{x}, \end{aligned} \quad (\text{A-19})$$

where \Im denotes the imaginary part. Taking the real part of both sides of this equation gives

$$\begin{aligned} & G_h(\mathbf{x}_A, \mathbf{x}_B, \omega) \\ &= \int_{\partial\mathbb{D}_0} \frac{2}{\omega\rho(\mathbf{x})} (\Re\{f_1(\mathbf{x}, \mathbf{x}_A, \omega)\} \partial_3 G_h(\mathbf{x}, \mathbf{x}_B, \omega) \\ &- \Re\{\partial_3 f_1(\mathbf{x}, \mathbf{x}_A, \omega)\} G_h(\mathbf{x}, \mathbf{x}_B, \omega)) d^2 \mathbf{x}. \end{aligned} \quad (\text{A-20})$$

This is the single-sided representation of the homogeneous Green's function. Using source–receiver reciprocity of the Green's functions gives

$$\begin{aligned} & G_h(\mathbf{x}_B, \mathbf{x}_A, \omega) \\ &= \int_{\partial\mathbb{D}_0} \frac{2}{\omega\rho(\mathbf{x})} (\partial_3 G_h(\mathbf{x}_B, \mathbf{x}, \omega) \Re\{f_1(\mathbf{x}, \mathbf{x}_A, \omega)\} \\ &- G_h(\mathbf{x}_B, \mathbf{x}, \omega) \Re\{\partial_3 f_1(\mathbf{x}, \mathbf{x}_A, \omega)\}) d^2 \mathbf{x}. \end{aligned} \quad (\text{A-21})$$

Note the analogy with the classical representation of the homogeneous Green's function formulated by equation (33).

We derive a simplified version of equation (A-21) by making, from here onward, again the assumption that the actual

medium at and above $\partial\mathbb{D}_0$ is homogeneous. For this situation, the Green's function $G(\mathbf{x}, \mathbf{x}_B, \omega)$ is upgoing at $\partial\mathbb{D}_0$; hence, $G(\mathbf{x}, \mathbf{x}_B, \omega) = G^-(\mathbf{x}, \mathbf{x}_B, \omega)$. To accommodate this, we apply decomposition to the wave fields at $\partial\mathbb{D}_0$ in equations (A-15) and (A-16) according to

$$\begin{aligned} & \int_{\mathbb{D}} \{p_A q_B - q_A p_B\} d^3\mathbf{x} \\ &= \int_{\partial\mathbb{D}_0} \frac{-2}{j\omega\rho} \{(\partial_3 p_A^+) p_B^- + (\partial_3 p_A^-) p_B^+\} d^2\mathbf{x} \\ &+ \int_{\partial\mathbb{D}_A} \frac{2}{j\omega\rho} \{(\partial_3 p_A^+) p_B^- + (\partial_3 p_A^-) p_B^+\} d^2\mathbf{x}, \quad (\text{A-22}) \end{aligned}$$

$$\begin{aligned} & \int_{\mathbb{D}} \{p_A^* q_B + q_A^* p_B\} d^3\mathbf{x} \\ &= \int_{\partial\mathbb{D}_0} \frac{-2}{j\omega\rho} \{(\partial_3 p_A^+)^* p_B^+ + (\partial_3 p_A^-)^* p_B^-\} d^2\mathbf{x} \\ &+ \int_{\partial\mathbb{D}_A} \frac{2}{j\omega\rho} \{(\partial_3 p_A^+)^* p_B^+ + (\partial_3 p_A^-)^* p_B^-\} d^2\mathbf{x}. \quad (\text{A-23}) \end{aligned}$$

Making the same substitutions as those mentioned below equations (A-15) and (A-16), using equations (A-7) and (A-8) and the additional condition that $p_B^+(\mathbf{x}, \omega) = G^+(\mathbf{x}, \mathbf{x}_B, \omega) = 0$ for \mathbf{x} at $\partial\mathbb{D}_0$, gives

$$\begin{aligned} & G^-(\mathbf{x}_A, \mathbf{x}_B, \omega) + H(x_{3,A} - x_{3,B}) f_1(\mathbf{x}_B, \mathbf{x}_A, \omega) \\ &= - \int_{\partial\mathbb{D}_0} \frac{2}{j\omega\rho(\mathbf{x})} \{ \partial_3 f_1^+(\mathbf{x}, \mathbf{x}_A, \omega) \} G^-(\mathbf{x}, \mathbf{x}_B, \omega) d^2\mathbf{x} \quad (\text{A-24}) \end{aligned}$$

and

$$\begin{aligned} & G^+(\mathbf{x}_A, \mathbf{x}_B, \omega) - H(x_{3,A} - x_{3,B}) f_1^*(\mathbf{x}_B, \mathbf{x}_A, \omega) \\ &= \int_{\partial\mathbb{D}_0} \frac{2}{j\omega\rho(\mathbf{x})} \{ \partial_3 f_1^-(\mathbf{x}, \mathbf{x}_A, \omega) \}^* G^-(\mathbf{x}, \mathbf{x}_B, \omega) d^2\mathbf{x}. \quad (\text{A-25}) \end{aligned}$$

Summing these two equations yields

$$\begin{aligned} & G(\mathbf{x}_A, \mathbf{x}_B, \omega) + H(x_{3,A} - x_{3,B}) 2j\Im\{f_1(\mathbf{x}_B, \mathbf{x}_A, \omega)\} \\ &= - \int_{\partial\mathbb{D}_0} \frac{2}{j\omega\rho(\mathbf{x})} \{ \partial_3 f_2(\mathbf{x}_A, \mathbf{x}, \omega) \} G(\mathbf{x}, \mathbf{x}_B, \omega) d^2\mathbf{x}, \quad (\text{A-26}) \end{aligned}$$

with $f_2(\mathbf{x}_A, \mathbf{x}, \omega)$ defined in equation (A-14) and where we used $G(\mathbf{x}, \mathbf{x}_B, \omega) = G^-(\mathbf{x}, \mathbf{x}_B, \omega)$ for \mathbf{x} at $\partial\mathbb{D}_0$. Taking the real part of both sides of equation (A-26) gives

$$\begin{aligned} & G_h(\mathbf{x}_A, \mathbf{x}_B, \omega) \\ &= -\Im \int_{\partial\mathbb{D}_0} \frac{4}{\omega\rho(\mathbf{x})} \{ \partial_3 f_2(\mathbf{x}_A, \mathbf{x}, \omega) \} G(\mathbf{x}, \mathbf{x}_B, \omega) d^2\mathbf{x}. \quad (\text{A-27}) \end{aligned}$$

Since at and above $\partial\mathbb{D}_0$ the medium is homogeneous, the derivative of $f_2(\mathbf{x}_A, \mathbf{x}, \omega)$ can be obtained via the wavenumber–frequency domain. To this end, we write, analogous to equation (A-14),

$$\begin{aligned} \tilde{f}_2(\mathbf{x}_A, \mathbf{k}_H, x_3, \omega) &= \tilde{f}_1^+(\mathbf{k}_H, x_3, \mathbf{x}_A, \omega) \\ &- \{ \tilde{f}_1^-(\mathbf{k}_H, x_3, \mathbf{x}_A, \omega) \}^*. \quad (\text{A-28}) \end{aligned}$$

Using $\partial_3 \tilde{f}_1^+ = -jk_3 \tilde{f}_1^+$ and $\partial_3 \tilde{f}_1^- = +jk_3 \tilde{f}_1^-$ (with k_3 defined below equation (A-3)), we find for real-valued k_3 (i.e., for non-evanescent waves),

$$\partial_3 \tilde{f}_2(\mathbf{x}_A, \mathbf{k}_H, x_3, \omega) = -jk_3 \tilde{f}_2(\mathbf{x}_A, \mathbf{k}_H, x_3, \omega). \quad (\text{A-29})$$